Newcastle University

School of Mathematics and Statistics

MAS8091 Project Report

Galactic Dynamo Action in Spherical Geometry

Author: James Hollins

Supervisors: Paul Bushby and Anvar Shukurov

Abstract

Dynamo theory has emerged as the most plausible explanation for the magnetic fields observed in astrophysical objects, such as stars, planets and galaxies [9]. This report applies mean-field dynamo theory to the magnetic fields of the halos of spiral galaxies by solving the mean-field dynamo equation in spherical geometry. The method of solution involves finding an eigenfunction expansion over free-decay modes, the Galerkin expansion. Two models will be discussed, a quasi-homogeneous spherical dynamo and a simple disc-halo dynamo. Dipolar and quadrupolar solutions of both $\alpha\omega$ and $\alpha^2\omega$ dynamos are discussed.

Contents

1 Introduction

1.1 Magnetic Fields

In a Scientific American article, E. N. Parker states the following about magnetic fields.

"Although only a small part of the available energy in the universe is invested in magnetic fields, they are responsible for most of the continual violent activity of the cosmos." (*Magnetic Fields in the Cosmos, Scientific American, Volume 249, 1983*)

Examples of violent activity driven by magnetic fields are the Aurora Borealis on Earth and stellar flares. Understanding these magnetic fields is important for explaining how they drive activity in the universe [9].

(a) The Aurora Borealis.
apod.nasa.gov/apod/ap130326.html

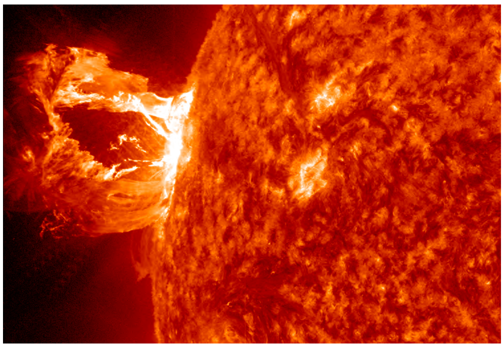

(b) A Solar Flare.
www.scientificamerican.com

Figure 1: Examples of processes in the universe driven by magnetic fields.

Magnetic fields are present in a wide variety of astrophysical objects, such as planets, stars and galaxies. Magnetic fields in the planets in the Solar system, with the exception of Venus and Mars, have been detected using magnetometers in spacecraft [9]. The magnetic fields of galaxies are detected using synchrotron emission, polarisation of electromagnetic radiation, Faraday rotation, Faraday depolarisation and the Zeeman effect [1].

The questions that then arise are how to explain the characteristics of these fields, such as the intensity and geometry. There exist two rival hypotheses to explain these phenomena. The first is that magnetic fields are primordial, trapped within astrophysical objects [9]. Whilst this hypothesis is attractively simple and can explain the origin of magnetic fields, it does not explain the strength, geometry or the lifetime of such fields. There also exists no suitable mechanism to explain how such fields were generated [11].

The second hypothesis is that the astrophysical objects where magnetic fields are present act as dynamos [9]. Dynamo action can be used to explain the characteristics of magnetic fields that cannot be accounted for by the primordial fields hypothesis [11]. Hence, this approach will be followed in the report.

1.2 Dynamos

1.2.1 A Laboratory Example

A dynamo converts the kinetic energy of an electrical conductor to electromagnetic energy. A simple dynamo can be constructed in a laboratory, consisting of a metal disc rotating on an axle over a conducting coil. The coil is aligned with the axle and is electrically connected to the disc and axle via brushes [9]. A schematic for such a dynamo is in Figure 2.

If a current is passed through the coil, a magnetic field is induced, aligned with the coil of wire. The electrons in the disc moving through the field experience a force directed along the radius of the disc, perpendicular to both the direction of the magnetic field and the motion of the electrons. The direction of the force can be found using the right-hand rule for vectors [9].

If the disc is rotating anti-clockwise when viewed from above and the magnetic field is directed upwards, an electromotive force is induced. This results in a current flowing from the axle to the edge of the disc. The current then flows through the brushes to the coil. This amplifies the magnetic field induced, increasing the current in the disc [9].

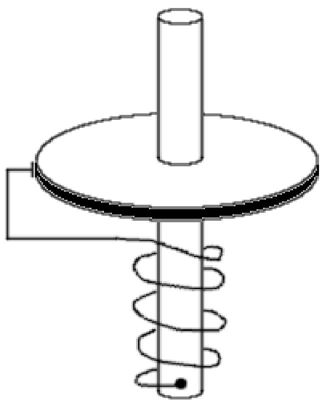

Figure 2: Schematic of a disc dynamo. The magnetic field is supplied by current flowing the loop of wire. Dynamos of this type are known as homopolar dynamos [5].
http://ffden-2.phys.uaf.edu/645fall2007_web.dir/Dan_S_dynamo_pages/

1.2.2 Astrophysical Dynamos

Astrophysical dynamos work on a similar principle. However, it is the motion of magnetically conducting fluid that generates the magnetic field. Electrons can move freely about the fluid, so we shall use an argument involving magnetic field lines rather than electromotive forces [9].

The number of integral lines (field lines) contained in a volume represents the strength of the magnetic field in the volume. Using a point made by Hannes Alfvén, a founder of magnetohydrodynamics, the field lines can be regarded as "frozen" in the fluid or "attached" to volume elements. The field moves with the fluid and is distorted by its motion. If the volume elements to which a field line is "attached" move at different speeds perpendicular to the field line, then the field line is stretched. This stretching of field lines corresponds to an increase in the strength of the field [9].

In mean-field dynamo theory, two effects can drive the dynamo [5]. The α effect is an electromotive force dependent on helicity, directed either parallel or antiparallel to the mean magnetic field. This is the results of small-scale turbulent motions with helicity [10]. The ω effect is caused by a shear as a result of differential rotation.In the $\alpha\omega$ dynamo, the α effect converts toroidal field to poloidal field, whilst the ω effect converts poloidal field to toroidal field [5]. These effects in the Sun are illustrated in Figure 3.

The result of both effects can be to increase the strength of the field. If these effects are strong enough to overcome dissipation, a dynamo occurs and the strength of the magnetic field increases [8]. In $\alpha^2\omega$ dynamos, both mechanisms operate for toroidal field generation [5].

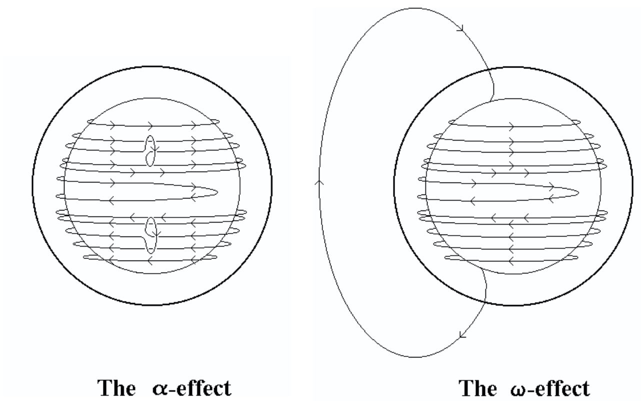

Figure 3: Illustration of the α and ω effects for the Solar dynamo. In the α effect, the toroidal field lines are twisted, whilst the poloidal field lines are stretched by differential rotation. In both effects, the field lines are stretched, which corresponds to an increase in magnetic field strength as discussed.

http://solarscience.msfc.nasa.gov/dynamo.shtml

1.3 Spiral Galaxies

1.3.1 Galactic Discs

Galaxies are collections of stars, bound by gravity. The length scales associated with such objects are usually measured in kiloparsecs (kpc), where 1 pc = 3.26 light-years= 3.086×10^{16} m. In disc galaxies, the stars are distributed throughout a spheroidal bulge and a disc. The flatness of the disc is a result of rapid rotation [11]. The interstellar medium (ISM) consists of gas and dust particles [3]. Spiral galaxies are disc galaxies with arms emerging from the central region. Often the pattern consists of two spirals, with a large degree of symmetry with respect to the galactic centre [7].

There is a large variation amongst the spiral structures observed in these galaxies. The most well defined spiral structure is called as grand-design spiral structure, consisting of two great arms. Examples of this are the galaxies M 51, M 81 and M 100. These grand-design structures are thought to be generated as a result of a rotating bar within the galaxy, or a perturbation resulting from the tidal gravitational field of a companion galaxy [3].

The other extreme of spiral structure is known as flocculent spiral structure, with short spiral arms. This structure is more commonly observed than the grand design structure. The origin of the spiral structure is not fully understood. It is known that the stars and gas in discs have small, random velocities. These irregularities can be amplified, which forms short spiral arms [3].

The rotational velocity of a galaxy $v_c(r)$ is defined as $v_c(r) \equiv r\Omega(r)$, where $\Omega(r)$ is the angular velocity. In the central region of the galaxy, $\Omega(r)$ is almost constant. This yields $v_c \propto r$, the distance from the galactic centre, which is similar to the rotational velocity of a solid body [3]. In the outer regions of spiral galaxies the rotation curve is flat, that is $v_c(r) =$ constant [7]. As a consequence, we can take $\Omega \propto r^{-1}$ in this region. This approximation can be assumed typically at distances $r \gtrsim 5\,\mathrm{kpc}$ from the galactic centre in spiral galaxies [11].

Much of the ISM mass is in the form of molecules. The most abundant is the hydrogen molecule H_2 [3]. The gas in the ISM is ionised by ultraviolet radiation (UV), X-rays and cosmic rays. In the different phases of the ISM, the degree to which the gas is ionised ranges from 30% to 100% [11]. A significant fraction of the interstellar space consists of plasma ($T > 10^6\,\mathrm{K}$) in which the hydrogen and helium are fully ionised [3]. The small effective mean free path of interstellar gas particles allows a fluid description for the motion of the interstellar gas to be justified [11].

The ISM is involved in turbulent motions driven by supernova stars (SN).

SN remnants consist of hot gas at high pressure that initially expand supersonically. Once the expansion velocity is similar to or lower than the speed of sound in the surrounding gas, a pressure disturbance propagates at a velocity greater than that of the expanding SN shell. This drives motion in the surrounding gas and a proportion of the remnant energy is converted into the kinetic energy of the ISM. The occurrence of supernovae at almost random times and positions results in random forces, which drive random motions in the ISM, leading to turbulence. Since the interstelllar gas can be described as an electrically conducting fluid that is both rotating and turbulent, we can describe the motion of the gas using magnetohydrodynamics (MHD) [11].

Magnetic fields have been detected in the discs of spiral galaxies, Section 1.3.3 [1]. MHD dynamo action has emerged as the most plausible explanation for magnetic fields in spiral galaxies whose scales exceed that of interstellar turbulence [2], this length scale is typically 0.05–0.1 kpc [11].

1.3.2 Galactic Halos

The galactic halo is one of the components of a spiral galaxy. The easily detectable halos consist of stars and gas orbiting at high velocities about the galactic centre [13]. The stars in the halo form an almost spherical distribution. In the Milky Way, it is observed that the stellar halo extends to at least 25 kpc from the galactic centre, whilst the stars in the disc do not extend to very large radii [3].

Hot gas from the disc flows to the halo in a convection type flow known as the galactic fountain. The fountain is driven by the collective energy input of tens of supernovae in clusters are commonly called OB associations. These clusters contain a high fraction of O and B type stars and are of 0.5–1 kpc in size [3, 11]. The temperature of the hot gas is sufficiently high for the gas to be fully ionised by gas particle collisions [11]. This gas contains magnetic fields in which the radius of the circular motion of the gas particles in the magnetic field, the Larmor radius, acts a mean free path, and so a fluid description can be applied to the motion of the gas [4, 11]. Hence, we shall adopt an MHD approach to describe the motion of the gas, as discussed previously.

Galactic halos have magnetic fields as discussed in Section 1.3.4, and observations reveal vertical field components in the halo that may be related to dynamo action [1]. Hence, we consider dynamo action in spherical geometry, as appropriate to modeling the magnetic fields of galactic halos.

1.3.3 Magnetic Fields in Galactic Discs

Two different systems of units are used in electromagnetism. In Gaussian units, magnetic field strength is measured in Gauss (G). In SI units, this quantity is measured in Teslas (T), where $1\,\mathrm{T} = 10^4\,\mathrm{G}$ [4]. The measurements quoted in this section are in Gauss.

Modeling surveys of the total synchrotron and γ-ray emission from the Milky Way yield a total field strength near the Sun of about $6\,\mu$G. This figure is in agreement with data from Voyager, in addition to data collected via observations of Zeeman splitting in low-density gas clouds and rotation measure data from pulsars. In the inner Galaxy the total field strength is about $10\,\mu$G. Measurements of the field strength near the Galactic Centre yield a measurement of $100\,\mu$G for the total magnetic field strength [1].

Measurements of the Voyager 2 spacecraft in the heliosheath, the region of the heliosphere at which the Solar wind has slowed to subsonic speeds, show that the strength of the surrounding magnetic field in the ISM is 4–5 μG. This field is oriented at an angle of about 30° from the Galactic plane. Voyager 1 has measured a field strength in interstellar space of $5.62 \pm 0.01\,\mu$G [1].

The strengths of external spiral galaxies have also been observed. Galaxies such as M 31 and M 33, which are radio-faint have field strengths of approximately $6\,\mu$G. Galaxies such as M 51, M 83 and NGC 6946, which are gas-rich with high star formation rates have field strengths in the range 15–20 μG [1].

Spiral fields in galactic discs are generated by either dynamo action, compression or shear in the interarm regions. Large-scale patterns of Faraday rotation measures can be identified via diffuse polarised emission of galactic discs or in rotation measure data from polarised background sources. These are signatures of $\alpha\omega$ dynamo action generating a regular magnetic field [1].

However, $\alpha\omega$ dynamo action cannot wholly account for the spiral pattern of magnetic fields. For example, the spiral pattern of M 51 cannot be explained fully by a regular field in the disc. In this case, a large proportion of the field is anisotropic turbulent and is better explained via compression and shear of non-axisymmetric gas flows [1].

1.3.4 Magnetic Fields in Galactic Halos

Nearby edge-on galaxies are observed to have a disc-parallel field near the disc plane. Vertical field components have been detected in the halos of NGC 253, NGC 891, NGC 4631 and NGC 5775, using polarised radio emission. These components form an X-shaped pattern, related to dynamo action assisted by an outflow [1].

The azimuthal symmetry of magnetic fields, corresponding to the field in the disc, is known for many spiral galaxies. The vertical symmetry of the magnetic field in the halo is more difficult to determine. Background rotation measures in the Large Magellanic Cloud (LMC) suggest a quadrupolar field. Observations of the vertical symmetries of NGC 891 and NGC 5775 suggest the vertical fields of these galaxies are quadrupolar [1].

In NGC 253, a halo extending to approximately 9 kpc above the galactic plane has been detected. The regular field detected is predominantly parallel to the plane in the disc and in the halo. The likely cause of this is strong differential rotation in the disc [2]. In addition, an outwards-directed helical field has been detected above the central starburst region in the gas outflow cone, using high-resolution rotation measure mapping. The strength of this field is approximately $20\,\mu$G and extends to at least 1 kpc in height [1]. In NGC 4631, the radio halo is of height $\simeq 2$ kpc. The magnetic field lines are almost perpendicular to the inner disc, which exhibits almost rigid rotation [2].

1.4 The Mean Field Dynamo Equation

1.4.1 Derivation

In a moving, electrically conducting medium with the assumption of isotropic conductivity, Ohm's law has the form

$$\mathbf{J} = \sigma(\mathbf{v} \times \mathbf{B} + \mathbf{E}), \tag{1.1}$$

where σ is electrical conductivity, $\mathbf{J}$ is the current density, $\mathbf{v}$ is the velocity of the conductor, $\mathbf{B}$ is the magnetic field and $\mathbf{E}$ is the electric field in the conductor [10]. The Maxwell equations in the MHD approximation have the form

$$\nabla \cdot \mathbf{E} = \frac{\rho_c}{\epsilon}, \tag{1.2a}$$

$$\nabla \cdot \mathbf{B} = 0, \tag{1.2b}$$

$$\nabla \times \mathbf{E} = -\frac{\partial \mathbf{B}}{\partial t}, \tag{1.2c}$$

$$\nabla \times \mathbf{B} = \mu \mathbf{J}, \tag{1.2d}$$

where ρ_c is the charge density, ϵ is the permittivity and μ is the permeability [10]. In MHD, the assumption is made that the fluid velocity is much less than the speed of light. As a consequence, the current displacement term in (1.2d) has been neglected [5]. Equations (1.1) and (1.2b-d) can be combined into the magnetic induction equation

$$\frac{\partial \mathbf{B}}{\partial t} = \nabla \times (\mathbf{v} \times \mathbf{B}) + \eta \nabla^2 \mathbf{B}, \tag{1.3}$$

where $\eta = 1/\mu\sigma$ is the magnetic diffusivity, taken to be constant [10]. We shall assume that $\mathbf{B}$ and $\mathbf{v}$ both exhibit large scale behaviour with small scale variations. Then the $\mathbf{B}$ and $\mathbf{v}$ fields can be split into mean and fluctuating components [5],

$$\mathbf{B} = \overline{\mathbf{B}} + \mathbf{B}^{'}, \quad \mathbf{v} = \overline{\mathbf{v}} + \mathbf{v}^{'}. \tag{1.4}$$

The Reynolds averaging rules can be applied as follows [5]

$$\overline{\mathbf{B_1} + \mathbf{B_2}} = \overline{\mathbf{B_1}} + \overline{\mathbf{B_2}}, \quad \overline{\mathbf{v_1} + \mathbf{v_2}} = \overline{\mathbf{v_1}} + \overline{\mathbf{v_2}}. \tag{1.5}$$

Average quantities are unchanged, hence

$$\overline{\overline{\mathbf{B}}} = \overline{\mathbf{B}}, \quad \overline{\overline{\mathbf{v}}} = \overline{\mathbf{v}}. \tag{1.6}$$

Then, averaging (1.4) yields

$$\overline{\mathbf{B}'} = 0, \quad \overline{\mathbf{v}'} = 0. \tag{1.7}$$

We also assume that averaging commutes with differentiation. Hence,

$$\overline{\frac{\partial \mathbf{B}}{\partial t}} = \frac{\partial \overline{\mathbf{B}}}{\partial t}, \quad \overline{\nabla \cdot \mathbf{B}} = \nabla \cdot \overline{\mathbf{B}}. \tag{1.8}$$

Thus, taking the average of (1.3) yields

$$\frac{\partial \overline{\mathbf{B}}}{\partial t} = \nabla \times (\overline{\mathbf{v} \times \mathbf{B}}) + \eta \nabla^2 \overline{\mathbf{B}}. \tag{1.9}$$

Now we evaluate the term $\overline{\mathbf{v} \times \mathbf{B}}$. Using (1.4) and (1.7),

$$\overline{\mathbf{v} \times \mathbf{B}} = \overline{\overline{\mathbf{v}} \times \overline{\mathbf{B}} + \overline{\mathbf{v}} \times \mathbf{B}' + \mathbf{v}' \times \overline{\mathbf{B}} + \mathbf{v}' \times \mathbf{B}'} = \overline{\mathbf{v}} \times \overline{\mathbf{B}} + \overline{\mathbf{v}' \times \mathbf{B}'}. \tag{1.10}$$

Substituting (1.10) into (1.9) yields

$$\frac{\partial \overline{\mathbf{B}}}{\partial t} = \nabla \times (\overline{\mathbf{v}} \times \overline{\mathbf{B}}) + \nabla \times \boldsymbol{\varepsilon} + \eta \nabla^2 \overline{\mathbf{B}}, \tag{1.11}$$

where

$$\boldsymbol{\varepsilon} = \overline{(\mathbf{v}' \times \mathbf{B}')}. \tag{1.12}$$

This term is the mean field e.m.f. (electromotive force) due to fluctuations. Subtracting (1.11) from (1.3) gives the equation determining the fluctuations $\mathbf{B}^{'}$ [10],

$$\frac{\partial \mathbf{B}^{'}}{\partial t} = \nabla \times (\overline{\mathbf{v}} \times \mathbf{B}^{'}) + \nabla \times (\mathbf{v}^{'} \times \overline{\mathbf{B}}) + \nabla \times G + \eta \nabla^2 \mathbf{B}^{'}, \tag{1.13}$$

where

$$G = \mathbf{v}^{'} \times \mathbf{B}^{'} - \overline{\mathbf{v}' \times \mathbf{B}'}. \tag{1.14}$$

Equation (1.13) is a linear equation for $\mathbf{B}^{'}$, with a source term $\nabla \times (\mathbf{v}^{'} \times \overline{\mathbf{B}})$, where $\mathbf{B}^{'}$ can be thought of as the sum of two terms; one which is independent of $\overline{\mathbf{B}}$, the other resulting from the action of the small-scale turbulent velocity $\mathbf{v}^{'}$ on the mean magnetic field $\overline{\mathbf{B}}$ [10]. We shall assume that

$$\varepsilon_i = \varepsilon^{(0)}{}_i + a_{ij}\overline{\mathbf{B}}_j + b_{ijk}\frac{\partial \overline{\mathbf{B}}_j}{\partial x_k}. \tag{1.15}$$

where a_{ij} and b_{ijk} are tensors depending on $\mathbf{v}^{'}$ and $\overline{\mathbf{v}}$ and $\varepsilon^0{}_i$ is independent of $\overline{\mathbf{B}}$. For simplicity, we also assume there is no mean motion, $\overline{\mathbf{v}} = 0$, and $\mathbf{v}^{'}$ corresponds to homogeneous, isotropic turbulence. Then using symmetry arguments, $\boldsymbol{\varepsilon}^{(0)} = \mathbf{0}$. Symmetry arguments also yield the following forms for a_{ij} and b_{ijk} [10]:

$$a_{ij} = \alpha(\mathbf{r})\delta_{ij}, \quad b_{ijk} = -\beta(\mathbf{r})\epsilon_{ijk}. \tag{1.16}$$

Using (1.16) in (1.11) yields the mean field dynamo equation

$$\frac{\partial \overline{\mathbf{B}}}{\partial t} = \nabla \times (\alpha \overline{\mathbf{B}}) + \nabla \times (\overline{\mathbf{v}} \times \overline{\mathbf{B}}) - \nabla \times (\beta \nabla \times \overline{\mathbf{B}}) + \eta \nabla^2 \overline{\mathbf{B}}. \tag{1.17}$$

The term involving β acts like a diffusive term. We shall assume β is also constant and using (1.2b), along with the following identity

$$\nabla \times \nabla \times \mathbf{B} = \nabla(\nabla \cdot \mathbf{B}) - \nabla^2 \mathbf{B},$$

we can write

$$-\nabla \times (\beta \nabla \times \mathbf{B}) = \beta \nabla^2 \mathbf{B}. \tag{1.18}$$

Therefore, we can write the mean field dynamo equation as follows

$$\frac{\partial \overline{\mathbf{B}}}{\partial t} = \nabla \times (\alpha \overline{\mathbf{B}}) + \nabla \times (\overline{\mathbf{v}} \times \overline{\mathbf{B}}) + \eta_\tau \nabla^2 \mathbf{B}. \tag{1.19}$$

where $\eta_\tau = \eta + \beta$ is the turbulent magnetic diffusivity. As a consequence of our earlier assumptions, we take η_τ to be constant.

1.4.2 Dimensionless Form

For convenience, we shall now drop the bars since every term in (1.19) is an average

$$\frac{\partial \mathbf{B}}{\partial t} = \nabla \times (\alpha \mathbf{B}) + \nabla \times (\mathbf{V} \times \mathbf{B}) + \eta_\tau \nabla^2 \mathbf{B}. \tag{1.20}$$

We shall make the variables dimensionless with the following scalings. We shall normalise length by the radius of the dynamo volume R and time by the diffusion time η_τ/R^2. Using the typical scales associated with galactic halos, $R = 10$–15 kpc and $\eta_\tau = (3$–$5) \times 10^{27}$cm s^2, we obtain $\eta_\tau/R^2 \approx (0.5$–$2) \times 10^{10}$ years. The velocity field $\mathbf{V}$ is the large scale velocity due to differential rotation, and so we shall write $\mathbf{V}$ as $\mathbf{V} = \boldsymbol{\Omega} \times \mathbf{r}$, where $\boldsymbol{\Omega}$ is the angular velocity. As a consequence, $\mathbf{V}$ can be normalised via normalising both $\boldsymbol{\Omega}$ and using the length scale. $\mathbf{\Omega}$ and α are normalised by their maximum values Ω_0 and α_0. Now we can introduce the following dimensionless variables and associated scalings:

$$\frac{\partial}{\partial t} = \frac{\eta_\tau}{R^2}\frac{\partial}{\partial t'}, \quad \nabla = \frac{1}{R}\nabla', \quad \alpha = \alpha_0\alpha', \quad \mathbf{V} = \Omega_0 R\mathbf{V}', \tag{1.21}$$

where the prime denotes dimensionless variable. Substituting these into Equation (1.20) yields

$$\frac{\partial \mathbf{B}'}{\partial t'} = \frac{\alpha_0 R}{\eta_\tau}\nabla \times (\alpha'\mathbf{B}') + \frac{\Omega_0 R^2}{\eta_\tau}\nabla \times (\mathbf{V}' \times \mathbf{B}') + \eta_\tau\nabla^2\mathbf{B}'. \tag{1.22}$$

Note that the magnetic field is made dimensionless by $\mathbf{B} = B_0\mathbf{B}'$, where B_0 is the typical scale of the magnetic field strength. However, B_0 does not appear in the dimensionless equation, as the equation is linear in $\mathbf{B}$. Since all the variables are dimensionless, we can drop the prime notation. We shall also introduce the following dimensionless parameters

$$R_\alpha = \frac{\alpha_0 R}{\eta_\tau}, \quad R_\omega = \frac{\Omega_0 R^2}{\eta_\tau}. \tag{1.23}$$

Therefore, we obtain the following dimensionless mean field dynamo equation

$$\frac{\partial \mathbf{B}}{\partial t} = R_\alpha\nabla \times (\alpha\mathbf{B}) + R_\omega\nabla \times (\mathbf{V} \times \mathbf{B}) + \nabla^2\mathbf{B}. \tag{1.24}$$

2 Free-Decay Modes

The kinematic dynamo problem is an eigenvalue problem with eigenvalues γ for eigenfunctions $\mathbf{B}(\mathbf{r})$. Hence, we shall assume the time dependence of the magnetic field is of the form $e^{\gamma t}$ and write (1.24) as follows

$$\gamma\mathbf{B} = R_\alpha\nabla \times (\alpha\mathbf{B}) + R_\omega\nabla \times (\mathbf{V} \times \mathbf{B}) + \eta_\tau\nabla^2\mathbf{B}. \tag{2.1}$$

Such an equation can be solved using an eigenfunction expansion over the modes of free decay, denoted as ${\mathbf{B}_i}^{(0)}(\mathbf{r})$, known as the Galerkin expansion. The free-decay modes are the solutions to (2.1) in the absence of our source terms. This equation is obtained from (2.1) by setting $R_\alpha = R_\omega = 0$

$$\gamma\mathbf{B} = \eta_\tau\nabla^2\mathbf{B}. \tag{2.2}$$

For each free-decay mode, the time dependence is of the form $\exp(\gamma_i t)$. Hence we shall write (2.2) for each free decay mode as follows

$$\nabla^2{\mathbf{B}_i}^{(0)} = \gamma_i{\mathbf{B}_i}^{(0)}, \tag{2.3}$$

where γ_i is the decay rate of the i'th mode. This equation is subject to the following boundary conditions [8],

$$[\mathbf{B}_i{}^{(0)}] = 0 \text{ on } r = 1,\ \mathbf{B}_i{}^{(0)} = O(r^{-3}) \text{ as } r \to \infty. \tag{2.4}$$

The square bracket notation denotes surface quantities. The first condition in (2.4) denotes that there is no variation of $\mathbf{B}_i{}^{(0)}$ across the boundary $r = 1$, and so all components of $\mathbf{B}_i{}^{(0)}$ are continuous at this boundary [8].

2.1 The Poloidal and Toroidal Potentials

Attempting to solve (2.3) with vectors is an unpleasant exercise. Fortunately, it is possible with the assumption of axisymmetry, $\partial/\partial\phi = 0$, to solve this equation in terms of scalars [6, 8].

We shall rewrite $\mathbf{B}$ in terms of a poloidal field represented by $\nabla \times \mathbf{A}$, where $\mathbf{A}$ is a vector potential, plus a toroidal field represented by $\mathbf{B}_T$ as shown below

$$\mathbf{B} = \nabla \times \mathbf{A} + \mathbf{B}_T. \tag{2.5}$$

The form in (2.5) retains the condition that $\mathbf{B}$ is divergence free, $\nabla \cdot \mathbf{B} = 0$ [6, 8]. The standard technique is to write these fields as the gradients of scalar potentials as follows

$$\mathbf{A} = -\mathbf{r}\times\nabla S, \quad \mathbf{B}_T = -\mathbf{r}\times\nabla T, \tag{2.6}$$

where $\mathbf{r} = (r, 0, 0)$. It can be shown that substituting (2.6) into (2.3) gives the following equations for S and T [6]

$$\frac{1}{r^2}\frac{\partial}{\partial r}\left(r^2\frac{\partial S}{\partial r}\right) + \frac{1}{r^2\sin\theta}\frac{\partial}{\partial\theta}\left(\sin\theta\frac{\partial S}{\partial\theta}\right) = \gamma S, \tag{2.7a}$$

$$\frac{1}{r^2}\frac{\partial}{\partial r}\left(r^2\frac{\partial T}{\partial r}\right) + \frac{1}{r^2\sin\theta}\frac{\partial}{\partial\theta}\left(\sin\theta\frac{\partial T}{\partial\theta}\right) = \gamma T. \tag{2.7b}$$

subject to [6]

$$T = 0,\ [S] = \partial S/\partial r = 0 \text{ on } r = 1,\ S = O(r^{-2}) \text{ as } r \to \infty. \tag{2.8}$$

2.2 Solutions of the Potential Equations

We shall solve these equations using separation of variables. The method shall be demonstrated for a general potential G, where $G = S_i$ or T_i. For G, (2.7) is shown below

$$\frac{1}{r^2}\frac{\partial}{\partial r}\left(r^2\frac{\partial G}{\partial r}\right) + \frac{1}{r^2\sin\theta}\frac{\partial}{\partial\theta}\left(\sin\theta\frac{\partial G}{\partial\theta}\right) - \gamma G = 0. \tag{2.9}$$

Using separation of variables we obtain two ODEs; Bessel's equation in r and Legendre's equation in θ

$$r^2\frac{d^2R}{dr^2} + 2r\frac{dR}{dr} - [\gamma r^2 + n(n+1)]R = 0, \tag{2.10a}$$
$$\frac{d}{d\theta}\left(\sin\theta\frac{d\Theta}{d\theta}\right) + n(n+1)\Theta\sin\theta = 0, \tag{2.10b}$$

where $n(n+1)$ is the separation constant. Applying the substitutions $x = \sqrt{-\gamma}r$ and $Q(x) = x^{1/2}R(x)$ to (2.10a) and $x = \cos(\theta)$ and $y(x) = \Theta(x)$ to (2.10b), we obtain

$$x^2\frac{d^2Q}{dx^2} + x\frac{dQ}{dx} + \left[x^2 - \left(n+\tfrac{1}{2}\right)^2\right]Q = 0, \tag{2.11a}$$
$$\frac{d}{dx}\left[(1-x^2)\frac{dy}{dx}\right] + n(n+1)y = 0. \tag{2.11b}$$

Both these equations can be solved using standard techniques. We obtain Bessel functions as the solutions to (2.11a) and Legendre polynomials as the solutions to (2.11b) [6, 8]. Now we can write the non-singular solutions of (2.7) as follows,

$$T = \sum_{n=1}^{\infty}\sum_{l} T_{nl}(r)P_n(\cos\theta)\exp(\gamma_{nl}t), \tag{2.12a}$$
$$S = R\sum_{n=1}^{\infty}\sum_{l} S_{nl}(r)P_n(\cos\theta)\exp(\gamma_{nl}t), \tag{2.12b}$$

where

$$T_{nl}(r) = \frac{c_{nl}}{\xi_{nl}\sqrt{r}}J_{n+1/2}(\xi_{nl}r), \tag{2.13a}$$
$$S_{nl}(r) = \frac{c_{nl}}{\xi_{nl}\sqrt{r}}J_{n+1/2}(\xi_{nl}r), \tag{2.13b}$$

with c_{nl} constants and

$$\xi_{nl} = \sqrt{-\gamma_{nl}}. \tag{2.14}$$

The index l is used to denote the zeros of the Bessel functions. The factor of R in (2.12b) is to ensure the dimensions of the solutions agree with those for S and T [6]. To satisfy the conditions in (2.8), it is necessary for T_{nl} and S_{nl} to satisfy the following conditions:

$$T_{nl} = 0,\ S_{nl} = a_n,\ \partial S_{nl}/\partial r = -(n+1)a_n \text{ on } r = 1. \tag{2.15}$$

where a_n is independent of r [6]. By eliminating a_n from the second and third conditions, we obtain the following boundary condition for S_{nl} [6]

$$\partial S_{nl}/\partial r + (n+1)S_{nl} = 0. \tag{2.16}$$

Using recurrence relations, and the requirement that T_{nl} and S_{nl} do not vanish simultaneously gives [6]

$$J_{n-1/2}(\xi_{nl})J_{n+1/2}(\xi_{nl}) = 0. \tag{2.17}$$

From this we can obtain values for ξ_{nl}. Using $\gamma_{nl} = -(\xi_{nl})^2$, we can obtain the decay rates γ_{nl} [6], shown in Table 1.

Table 1: Decay rates γ_{nl}.

	$n = 1$	$n = 2$	$n = 3$	$n = 4$
$l = 1$	$-\pi^2$	$-(4.493)^2$	$-(2\pi)^2$	$-(7.725)^2$
$l = 2$	$-(4.493)^2$	$-(5.763)^2$	$-(7.725)^2$	$-(9.095)^2$
$l = 3$	$-(5.763)^2$	$-(6.988)^2$	$-(9.095)^2$	$-(10.417)^2$
$l = 4$	$-(6.988)^2$	$-(8.813)^2$	$-(10.417)^2$	$-(11.705)^2$

For n odd, $J_{n-1/2}(\xi_{nl}) = 0$ for all l. Hence, $T_{nl} = 0$ for n odd. Conversely, when n is even, $J_{n+1/2}(\xi_{nl}) = 0$ for all l. Hence, $S_{nl} = 0$ for n even. Now the solutions satisfying (2.15) can be written, with $j = n + l$, as follows

$$T = \sum_{j=3}^{\infty} \sum_{k\,\mathrm{even}} \frac{c_{k(j-k)}}{\sqrt{r}} J_{k+1/2}(\xi_{k(j-k)} r) P_{(j-k)}(\cos\theta) \exp(\gamma_{k(j-k)} t), \tag{2.18a}$$

$$S = \sum_{j=2}^{\infty} \sum_{k\,\mathrm{odd}} \frac{d_{k(j-k)}}{\sqrt{r}} J_{k+1/2}(\xi_{k(j-k)} r) P_{(j-k)}(\cos\theta) \exp(\gamma_{k(j-k)} t), \tag{2.18b}$$

where $c_{k(j-k)}$ and $d_{k(j-k)}$ are constants. The sums are arranged to be ordered in terms of the decay rates, $|\gamma|$.

Using (2.5), (2.6) and (2.18) we can write the free-decay modes using these potentials. These form two sets based on their symmetries about the mid-plane $\theta = \pi/2$, called the antisymmetric and symmetric modes respectively. The antisymmetric modes are derived from S_{nl} and T_{nl} for $n + l$ even and correspond to the modes of dipolar parity, whilst the symmetric modes are derived from S_{nl} and T_{nl} for $n + l$ odd and correspond to the modes of a quadrupolar parity.

The first four antisymmetric and the first four symmetric modes are given in Section 2.3, denoted by $\mathbf{B}_i{}^{(0)\mathrm{a}}$ and $\mathbf{B}_i{}^{(0)\mathrm{s}}$ to distinguish the symmetries. These modes have been normalised to form an orthonormal set of basis functions. It should be noted that the modes are either purely poloidal or toroidal.

2.3 The Free Decay Modes

2.3.1 The Antisymmetric Modes

The mode ${\bf B_1}^{(0)\rm a}$ is purely poloidal with the eigenvalue ${\gamma_1}^a = -\pi^2$:

$$ {\bf B_1}^{(0)\rm a} = C_1 \left\{ \frac{2}{r} Q_1(r)\cos\theta, -\frac{\sin\theta}{r}\frac{d}{dr}[rQ_1(r)], 0 \right\}, \tag{2.19a} $$

$$ C_1 \approx 0.346,\ Q_1(r) = r^{-1/2} J_{3/2}(k_1 r),\ k_1 = \pi. \tag{2.19b} $$

The modes ${\bf B_2}^{(0)\rm a}$ and ${\bf B_3}^{(0)\rm a}$ form a degenerate pair, with eigenvalue ${\gamma_2}^a = -(5.763)^2$. ${\bf B_2}^{(0)\rm a}$ is purely poloidal, whilst ${\bf B_3}^{(0)\rm a}$ is purely toroidal:

$$ {\bf B_2}^{(0)\rm a} = C_2 \left\{ \frac{2}{r} Q_2(r)\cos\theta(5\cos2\theta - 1), -\frac{\sin\theta}{r}(5\cos^2\theta - 1)\frac{d}{dr}[rQ_2(r)], 0 \right\}, \tag{2.20a} $$

$$ C_2 \approx 0.250,\ Q_2(r) = r^{-1/2} J_{7/2}(k_2 r),\ k_2 \approx 5.763, \tag{2.20b} $$

$$ {\bf B_3}^{(0)\rm a} = C_3 \left\{ 0, 0, Q_3(r)\sin\theta\cos\theta \right\}, \tag{2.21a} $$

$$ C_3 \approx 3.445,\ Q_3(r) = r^{-1/2} J_{5/2}(k_2 r). \tag{2.21b} $$

The mode ${\bf B_4}^{(0)\rm a}$ is purely poloidal with the eigenvalue ${\gamma_4}^a = -(2\pi)^2$:

$$ {\bf B_4}^{(0)\rm a} = C_4 \left\{ \frac{2}{r} Q_4(r)\cos\theta, -\frac{\sin\theta}{r}\frac{d}{dr}[rQ_4(r)], 0 \right\}, \tag{2.22a} $$

$$ C_4 \approx 0.346,\ Q_4(r) = r^{-1/2} J_{3/2}(k_4 r),\ k_4 = 2\pi. \tag{2.22b} $$

Plots of the antisymmetric modes are given in Figure 4, shown in the (x, z)–plane for convenience.

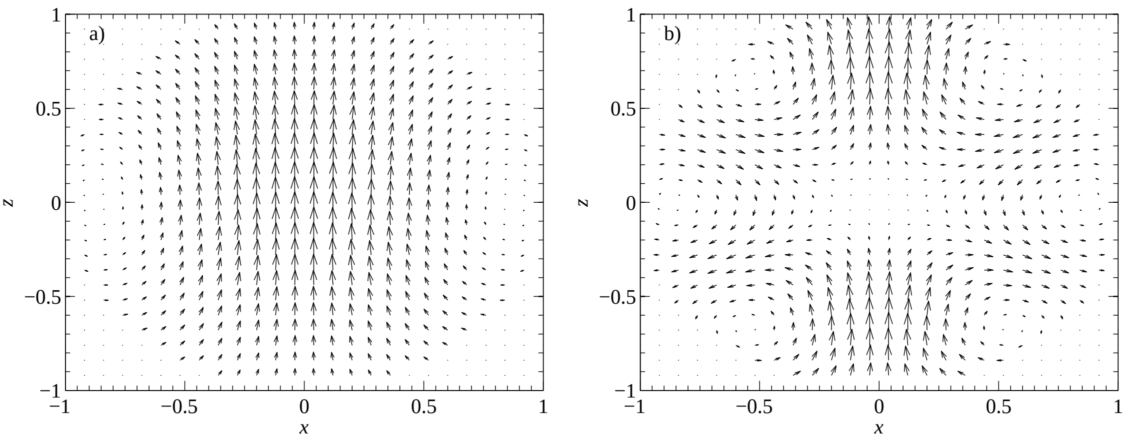

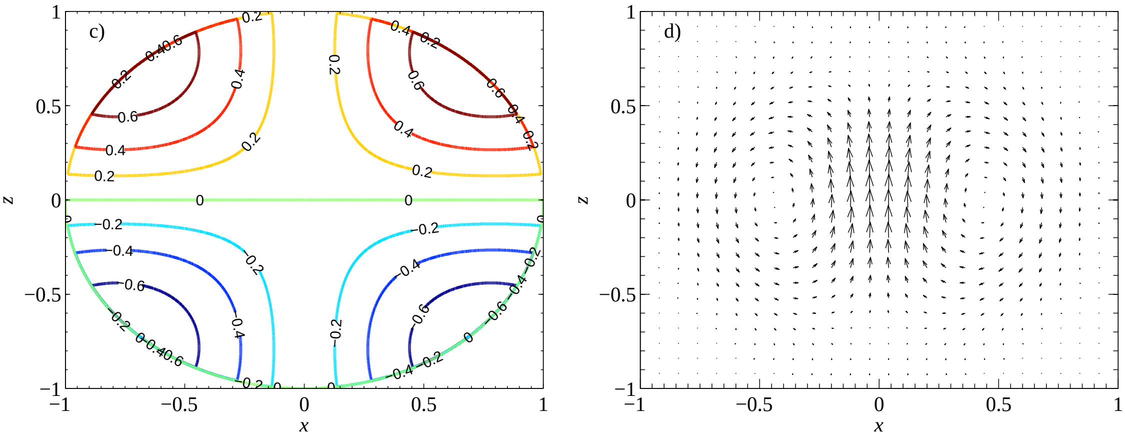

Figure 4: The antisymmetric free decay modes: a) $\mathbf{B_1}^{(0)\mathrm{a}}$, b) $\mathbf{B_2}^{(0)\mathrm{a}}$, c) $\mathbf{B_3}^{(0)\mathrm{a}}$ and d) $\mathbf{B_4}^{(0)\mathrm{a}}$. The poloidal modes are represented via vectors, the length of which are proportional to $|\mathbf{B}_i{}^{(0)\mathrm{a}}|$. The toroidal mode is represented via contours. The red and yellow curves denote the isolines for $B_\phi > 0$, the green curves indicate the isolines for $B_\phi = 0$, whilst the blue curves denote the isolines for $B_\phi < 0$. The isolines are drawn for values of 0, ±0.2, ±0.4 and ±0.6.

2.3.2 The Symmetric Modes

The modes $\mathbf{B}_1{}^{(0)_s}$ and $\mathbf{B}_2{}^{(0)_s}$ form a degenerate eigenfunction pair, with eigenvalue $\gamma_1{}^s = -(4.493)^2$. $\mathbf{B}_1{}^{(0)_s}$ is a purely poloidal mode, whilst $\mathbf{B}_2{}^{(0)_s}$ is a purely toroidal mode:

$$\mathbf{B}_1{}^{(0)_s} = A_1\left\{r^{-1}P_1(r)(3\cos^2\theta - 1), -r^{-1}\sin\theta\cos\theta\frac{d}{dr}[rP_1(r)], 0\right\}, \tag{2.23a}$$

$$\text{where } A_1 \approx 0.662,\ P_1(r) = r^{-1/2}J_{5/2}(q_1 r),\ q_1 \approx 4.493. \tag{2.23b}$$

$$\mathbf{B}_2{}^{(0)_s} = A_2\left\{0, 0, P_2(r)\sin\theta\right\}, \tag{2.24a}$$

$$\text{where } A_2 \approx 1.330,\ P_2(r) = r^{-1/2}J_{3/2}(q_1 r). \tag{2.24b}$$

The modes $\mathbf{B}_3{}^{(0)_s}$ and $\mathbf{B}_4{}^{(0)_s}$ form a degenerate eigenfunction pair, with eigenvalue $\gamma_3{}^s = -(6.988)^2$. $\mathbf{B}_3{}^{(0)_s}$ is a purely poloidal mode, whilst $\mathbf{B}_4{}^{(0)_s}$ is a purely toroidal mode:

$$\mathbf{B}_3{}^{(0)_s} = A_3\left\{r^{-1}P_3(r)S_1(\theta), r^{-1}\frac{d}{dr}[rP_3(r)]\frac{d}{d\theta}S_1(\theta), 0\right\}, \tag{2.25a}$$

$$\text{where } A_3 \approx 0.133,\ P_3(r) = r^{-1/2}J_{9/2}(q_3 r), q_3 \approx 6.988,\ S_1(\theta) = 35\cos^4\theta - 30\cos^2\theta + 3, \tag{2.25b}$$

$$\mathbf{B}_4{}^{(0)_s} = A_4\left\{0, 0, -P_4(r)\frac{d}{d\theta}S_2(\theta)\right\}, \tag{2.26a}$$

$$\text{where } A_4 \approx 0.763,\ P_4(r) = r^{-1/2}J_{7/2}(q_3 r),\ S_2(\theta) = 5\cos^3\theta - 3\cos\theta. \tag{2.26b}$$

Plots of the symmetric modes are given below, again shown in the (x, z)–plane for convenience.

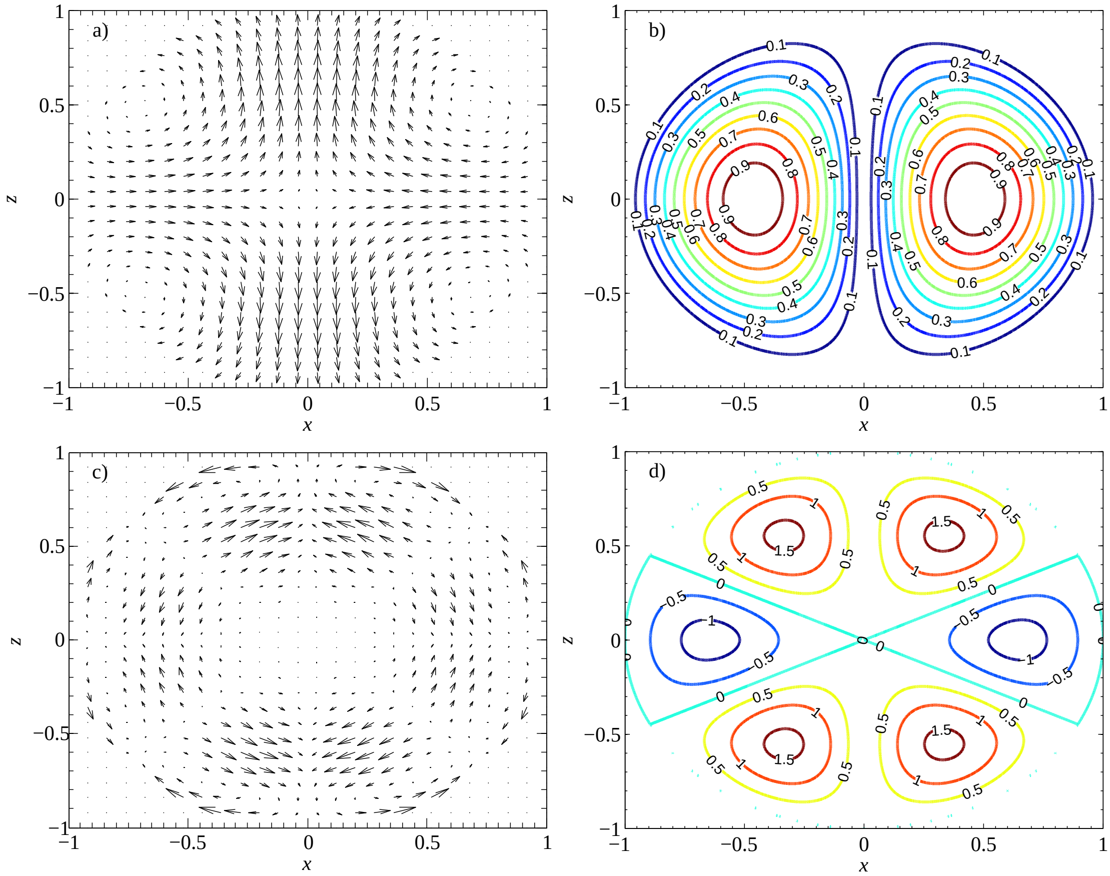

Figure 5: The symmetric free decay modes: a) $\mathbf{B}_1{}^{(0)\mathrm{s}}$, b) $\mathbf{B}_2{}^{(0)\mathrm{s}}$, c) $\mathbf{B}_3{}^{(0)\mathrm{s}}$ and d) $\mathbf{B}_4{}^{(0)\mathrm{s}}$. The poloidal modes are represented via vectors, the length of which are proportional to $|\mathbf{B}_i{}^{(0)\mathrm{s}}|$. The toroidal modes are represented via contours. For $\mathbf{B}_2{}^{(0)\mathrm{s}}$, the isolines are drawn for increments of 0.1. The dark red curves denote the isolines $B_\phi = 0.9$, whilst the black curves denote the isolines for $B_\phi = 0.1$. Whereas for $\mathbf{B}_4{}^{(0)\mathrm{s}}$, the blue curves indicate the isolines for $B_\phi < 0$, the cyan curves indicate the isolines for $B_\phi = 0$, whilst the red and yellow curves indicate the isolines for $B_\phi > 0$. The isolines are drawn for the values 0, ± 0.5, ± 1 and 1.5.

3 The Galerkin Expansion

The free decay modes form an orthonormal set of basis functions, and solutions of the mean-field dynamo equation can be expanded over them

$$\mathbf{B} = \exp(\Gamma t) \sum_{i=1}^{N} a_i \mathbf{B}_i{}^{(0)}(\mathbf{r}) \tag{3.1}$$

where N is the number of free decay modes used in the expansion. Since the free decay modes satisfy the vacuum boundary conditions, $\mathbf{B}$ also satisfies these conditions.

Substituting (3.1) into (2.1) and integrating over space yields a system of algebraic equations for a_i:

$$a_j(\gamma_j - \Gamma) + \sum_{\substack{i=1 \\ i \neq j}}^{N} a_i W_{ji} = 0, \quad \text{for} \quad j = 1, 2, \ldots, N, \tag{3.2}$$

with matrix elements W_{ji} defined as

$$W_{ji} = \int \mathbf{B}_j{}^{(0)} \cdot \widehat{\mathcal{W}} \mathbf{B}_i{}^{(0)} \, d^3\mathbf{r}. \tag{3.3}$$

This integration is performed over the whole space. We shall consider both the $\alpha\omega$ and $\alpha^2\omega$ dynamos in this report. For the $\alpha^2\omega$ dynamo, the perturbation operator $\widehat{\mathcal{W}}$ is defined as

$$\widehat{\mathcal{W}}\mathbf{B} = R_\alpha \nabla \times (\alpha \mathbf{B}) + R_\omega \nabla \times (\mathbf{V} \times \mathbf{B}), \tag{3.4}$$

whilst for the $\alpha\omega$ dynamo, $\widehat{\mathcal{W}}$ is given by

$$\widehat{\mathcal{W}}\mathbf{B} = R_\alpha(\nabla \times (\alpha \mathbf{B}) - [\nabla \times (\alpha \mathbf{B})]_\phi) + R_\alpha \nabla \times (\mathbf{V} \times \mathbf{B}). \tag{3.5}$$

A discussion of the two dynamo mechanisms can be found in Section 4.1. Since $\mathbf{V} = \mathbf{\Omega} \times \mathbf{r}$, the rotational only has an azimuthal component. Also, if $\alpha(\mathbf{r})$ is odd in θ and $\mathbf{V}(\mathbf{r})$ is even in θ, $\widehat{\mathcal{W}}$ preserves the division of the solutions into independent sets of symmetric and antisymmetric modes also for R_α,$R_\omega \neq 0$. We shall consider forms of $\alpha(\mathbf{r})$ and $\mathbf{V}(\mathbf{r})$ with these symmetries in θ in this report.

The symmetric and antisymmetric solutions will be considered independently. Each corresponding subset of symmetric and antisymmetric free decay modes represents a complete orthonormal functional basis. For axisymmetric $\alpha(\mathbf{r})$ and $\mathbf{V}(\mathbf{r})$, the modes with different azimuthal wavenumbers evolve independently of each other. Hence for simplicity, $\alpha(\mathbf{r})$ and $\mathbf{V}(\mathbf{r})$ are chosen to be aximsymmetric.

Since we assume axial symmetry, $\widehat{\mathcal{W}}$ transforms a purely poloidal field into a purely toroidal field and vice versa. Hence, the nonzero matrix elements occur when one of the fields ${\mathbf{B}_i}^{(0)}$ and ${\mathbf{B}_j}^{(0)}$ is poloidal and the other is toroidal. Since the toroidal fields vanish outside the conducting sphere, the integration in (3.3) is restricted to the region r ≤ 1.

The model considered must satisfy the necessary conditions for dynamo action to occur. This means that toroidal and poloidal fields are mixed for $R_\alpha, R_\omega \neq 0$ and the growing field is neither purely poloidal or toroidal. Since the modes are either purely poloidal or toroidal, we must include at least one mode of each symmetry. However, the first three antisymmetric modes are required for $\alpha\omega$ dynamo to result in a growing dipolar field, since ${\mathbf{B}_2}^{(0)\mathrm{a}}$ and ${\mathbf{B}_3}^{(0)\mathrm{a}}$ form a degenerate pair. Thus, we are forced to include at least three antisymmetric modes. We shall also include the mode ${\mathbf{B}_4}^{(0)\mathrm{a}}$ to improve accuracy and also for comparison to the symmetric modes, since the symmetric modes form degenerate pairs. Hence, we shall set $N = 4$ as the minimum number of modes to include to obtain a growing magnetic field.

The system in (3.2) has nontrivial solutions for a_i if its determinant equals zero. This yields an N'th-order algebraic equation for the growth rate Γ. Since $N = 4$, the equation for Γ is an fourth-order equation that can easily solved numerically.

The expansion coefficients are then found as the associated eigenvector for the largest value of Γ, the dominant growth rate. Any $N-1$ coefficients a_i can be expressed using the remaining coefficient, e.g. a_1, with this coefficient fixed by the normalisation condition $\sum_i |a_i|^2 = 1$.

4 Quasi-Homogeneous Dynamo

Since the intended application of our model is to galactic halos, we choose the rotation to be cylindrically symmetric with a flat rotation curve at some distance from the axis of rotation. Thus, we adopt the following form for $\mathbf{V}$,

$$\mathbf{V} = [0, 0, V(s)], \tag{4.1}$$

where s is the cylindrical radius and

$$V(s) = V_0 \left[1 - \exp\left(\frac{-s}{s_0} \right) \right]. \tag{4.2}$$

In terms of spherical coordinates we have

$$V(r, \theta) = V_0 \left[1 - \exp\left(\frac{-r \sin\theta}{s_0} \right) \right]. \tag{4.3}$$

Here, s_0 is the characteristic radial scale of the disc. We incorporate V_0 into R_ω in order to normalise $\mathbf{V}(\mathbf{r})$ via the relation $\Omega_0 = V_0/s_0$. For numerical estimates, we adopt values typical of spiral galaxies $s_0 = 5$ kpc, $R = 10$ kpc and $\eta_T = 5 \times 10^{27}\text{cm}^2\text{s}^{-1}$. To simplify the exploration of the parameter space, R_α will be the sole control parameter. We shall consider R_α in the range $0 \leq R_\alpha \leq 10$, a commonly used range for R_α in galaxies. The strength of the differential rotation is fixed at $R_\omega = 200$, which corresponds to $V_0 = 167\,\text{kms}^{-1}$. This is motivated by the fact that the rotation of galaxies can be well determined from observations, whilst R_α is obtained from order of magnitude estimates [11]. We shall assume a simple form for the normalised α coefficient $\alpha(\mathbf{r}) = \cos\theta$.

4.1 The $\alpha^2\omega$ and $\alpha\omega$ Dynamos

We shall now briefly discuss the difference between the $\alpha^2\omega$ and $\alpha\omega$ dynamos. Since we have taken a cylindrical rotation law, we shall use cylindrical polar co-ordinates for the explanations in this section. It is convenient to write the magnetic and velocity fields as sums of poloidal and toroidal parts [8]

$$\mathbf{B} = \mathbf{B}_P + \mathbf{B}_T, \quad \mathbf{V} = \mathbf{V}_P + \mathbf{V}_T, \tag{4.4}$$

where $\mathbf{B}_P$ and $\mathbf{B}_T$ denote the poloidal and toroidal magnetic fields, similar to Section 2.1 but with $\mathbf{B}_P = \nabla \times \mathbf{A}$ representing the poloidal field. $\mathbf{V}_P$ and $\mathbf{V}_T$ are the poloidal and toroidal velocity fields. Since the velocity field considered is purely azimuthal, $\mathbf{V}_P = \mathbf{0}$ and we can write

$$\mathbf{V} = \mathbf{V}_T = s\Omega\hat{\phi}, \tag{4.5}$$

where Ω is the angular velocity [8]. With

$$\mathbf{A} = (0, 0, A), \quad \mathbf{B}_T = (0, 0, B), \tag{4.6}$$

(4.4) yields the following equations [8]

$$\frac{\partial B}{\partial t} = s(\mathbf{B}_P \cdot \nabla)\Omega + \nabla \times (\alpha \mathbf{B}_P) + \eta_\tau \left(\nabla^2 - \frac{1}{s^2}\right) B, \tag{4.7}$$

$$\frac{\partial A}{\partial t} = \alpha B + \eta_\tau \left(\nabla^2 - \frac{1}{s^2}\right) A. \tag{4.8}$$

These are the equations for the $\alpha^2\omega$ dynamo The α effect acts as a source for both poloidal and toroidal fields, via the terms involving α in (4.7) and (4.8) [5]. The differential rotation acts as an additional source term for the toroidal field, via $s(\mathbf{B}_P \cdot \nabla)\Omega$ in (4.7).

We can derive the $\alpha\omega$ dynamo equations are by first taking an order of magnitude estimate for the ratio of the two source terms in (4.7)

$$\left|\frac{s(\mathbf{B}_P\cdot\nabla)\Omega}{\nabla\times(\alpha\mathbf{B}_P)}\right| \sim \frac{L\Omega_0}{\alpha_0}, \tag{4.9}$$

where α_0 and Ω_0 are typical values of α and Ω [8]. The $\alpha\omega$ approximation applies when the differential rotation term dominates, $|\alpha_0| \ll |L\Omega_0|$ [8]. As a consequence, we can ignore the $\nabla \times (\alpha\mathbf{B}_P)$ term in (4.7) and obtain the following equation

$$\frac{\partial B}{\partial t} = s(\mathbf{B}_P \cdot \nabla)\Omega + \eta_\tau \left(\nabla^2 - \frac{1}{s^2}\right) B, \tag{4.10}$$

This equation along with (4.8) are the $\alpha\omega$ dynamo equations. The α effect is the source for the poloidal field only and differential rotation is the only source of the toroidal field [8].

For the $\alpha^2\omega$ dynamo we adopt the form for $\widehat{\mathcal{W}}$ given in (3.4), whereas the form in (3.5) corresponds to the $\alpha\omega$ dynamo.

4.2 $\alpha^2\omega$ Dynamo

4.2.1 Antisymmetric Modes

Our analysis shall focus on the eigenvalue Γ with the largest real part, as it corresponds to the most rapidly growing field. The dependence of the growth rate Re Γ and associated oscillation frequency Im Γ of the four antisymmetric modes on R_α are shown in Figure 6.

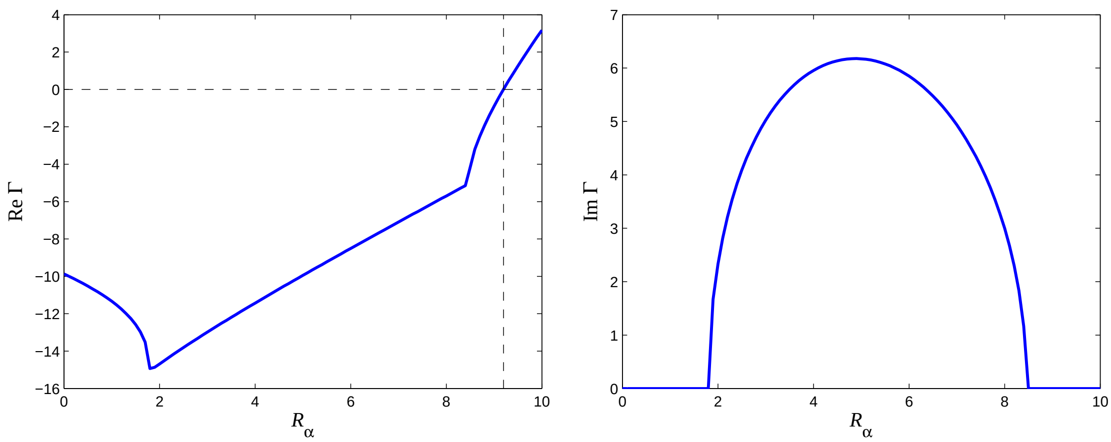

Figure 6: The dominant growth rate Re Γ and associated oscillation frequency Im Γ against R_α for the antisymmetric modes. The vertical dashed line denotes $R_{\alpha\,\mathrm{cr}}$, the value at which dynamo action produces a growing magnetic field.

The growth rate initially decreases with increasing R_α, but there is a turning point at $R_\alpha \approx 2$ at which Re Γ begins increasing, at an especially rapid rate for $R_\alpha > 8$. The growth threshold for the antisymmetric modes, corresponding to Re $\Gamma = 0$ is $R_{\alpha\,\mathrm{cr}} \approx 9.2$.

At small values of R_α, Im Γ is zero and the magnetic field evolves monotonically. As the growth rate begins to increase, the modes become oscillatory, with the maximum oscillation frequency at $R_\alpha \approx 5$. Near the generation threshold $R_\alpha \approx R_{\alpha\,\mathrm{cr}}$, Γ is real and the growing mode is stationary. Figure 6 suggests that the structure of the dominant mode changes at $R_\alpha \approx 2$ and at $R_\alpha \approx 8$.

This suggestion is confirmed by the dependence of the moduli of the expansion coefficients $|a_i|$ on R_α, shown in Figure 7.

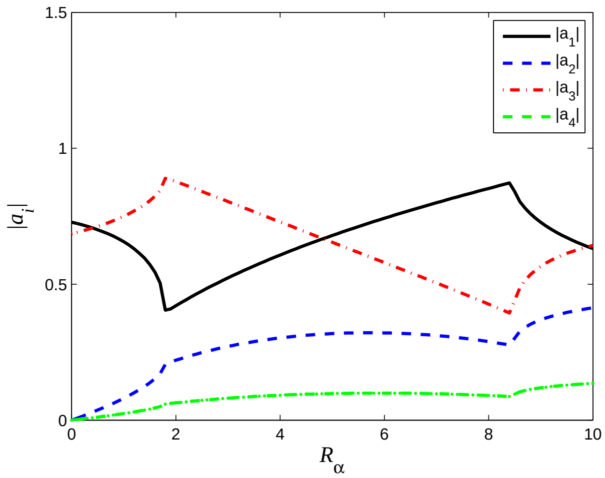

Figure 7: The expansion coefficients $|a_i|$ against R_α: $|a_1|$ (solid, black), $|a_2|$ (dashed, blue), $|a_3|$ (dashed, red), $|a_4|$ (dashed, green). For each value of R_α, the coefficients are normalised as discussed.

The mode $\mathbf{B}_3{}^{(0)\mathrm{a}}$ dominates for small R_α values, with the mode $\mathbf{B}_1{}^{(0)\mathrm{a}}$ becoming dominant in the range $2 \leq R_\alpha \leq 8$, where the modes are oscillatory. At $R_\alpha \approx 8$ where Γ is purely real, $\mathbf{B}_1{}^{(0)\mathrm{a}}$ becomes less dominant and the other modes become gradually more significant as R_α increases. The mode $\mathbf{B}_3{}^{(0)\mathrm{a}}$ becomes dominant just above the growth threshold $R_{\alpha\,\mathrm{cr}}$.

Figure 8 shows the poloidal structure of the solution at $R_\alpha = R_{\alpha\,\mathrm{cr}}$. The structure of the toroidal field at $R_\alpha = R_{\alpha\,\mathrm{cr}}$ is not shown, since it is the same as the free decay mode $\mathbf{B}_3{}^{(0)\mathrm{a}}$, as $\mathbf{B}_3{}^{(0)\mathrm{a}}$ is the only antisymmetric mode toroidal mode used in the solution.

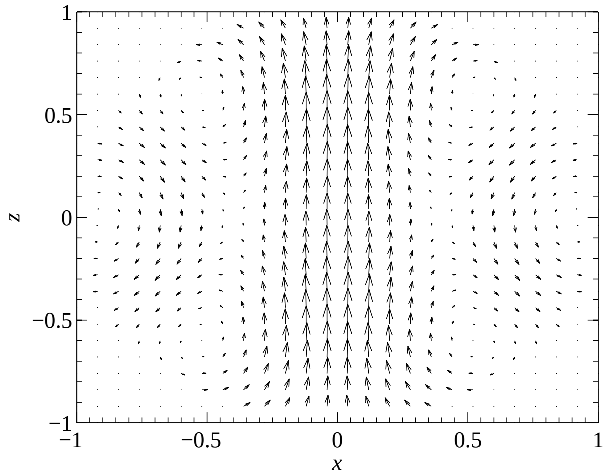

Figure 8: Magnetic field vectors in the (x, z)–plane of the dipolar poloidal field at $R_{\alpha\,\mathrm{cr}} \approx 9.2$ for the $\alpha^2\omega$ dynamo. The vector length is proportional to $|\mathbf{B}|$.

The poloidal structure of the magnetic field at $R_\alpha = R_{\alpha\,cr}$ is very similar to the mode $\mathbf{B}_1{}^{(0)_a}$ shown in Figure 4. This might be expected, since $\mathbf{B}_1{}^{(0)\mathrm{a}}$ is the dominant poloidal mode at $R_\alpha = R_{\alpha\,cr}$. There are some differences in the structure of the eigenfunction for $|x| > 0.5$, where it is more similar to that of the mode $\mathbf{B}_2{}^{(0)\mathrm{a}}$, showing that this mode has some significance in the structure of the field at the onset of dynamo action.

4.2.2 Symmetric Modes

We now consider the symmetric modes. The dependence of Re Γ on R_α for the four symmetric modes is shown in Figure 9.

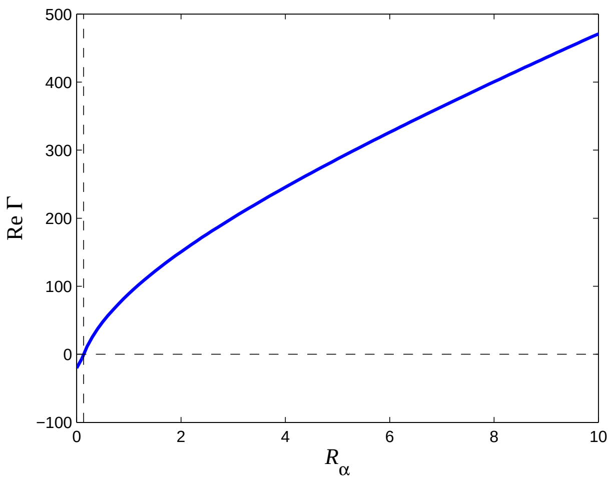

Figure 9: The dominant growth rate Re Γ against R_α for the symmetric modes. As for Figure 6, the vertical dashed line denotes $R_{\alpha\,\mathrm{cr}}$. For all R_α, Im $\Gamma = 0$.

In comparison to the antisymmetric modes, the growth rate increases much more rapidly with R_α. The growth threshold for the symmetric modes is $R_{\alpha\,\mathrm{cr}} \approx 0.14$, significantly lower than for the antisymmetric modes. Hence the preferred symmetry for the $\alpha^2\omega$ dynamo is quadrupolar. This contrasts with other spherical systems such as planets and stars, where the magnetic fields are usually dipolar [11]. The likely cause of this is the cylindrical symmetry of the rotational velocity.

The oscillation frequency is zero for all R_α and so the growing symmetric mode is stationary. The dependence of the moduli of the expansion coefficients $|a_i|$ on R_α is shown in Figure 10.

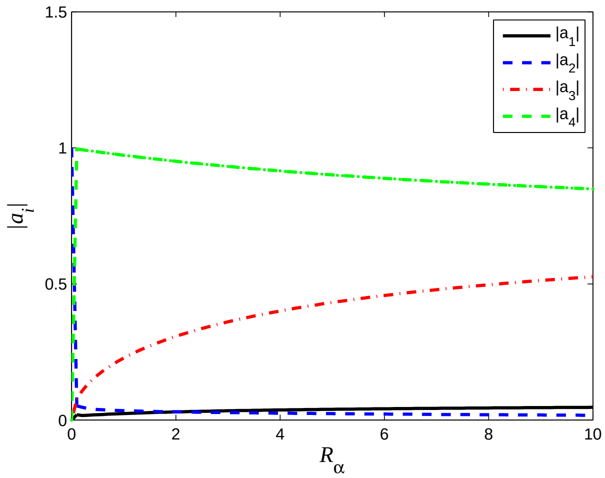

Figure 10: The expansion coefficients $|a_i|$ against R_α: $|a_1|$ (solid, black), $|a_2|$ (dashed, blue), $|a_3|$ (dashed, red), $|a_4|$ (dashed, green). For each value of R_α, the coefficients are normalised as discussed.

We see that, except for very small R_α where $\mathbf{B}_2{}^{(0)\mathrm{s}}$ is dominant, $\mathbf{B}_4{}^{(0)\mathrm{s}}$ is the dominant mode. $\mathbf{B}_3{}^{(0)\mathrm{s}}$ increases in significance with increasing $R_{\alpha\,\mathrm{cr}}$. Throughout the majority of the range for R_α, the modes $\mathbf{B}_1{}^{(0)\mathrm{s}}$ and $\mathbf{B}_2{}^{(0)\mathrm{s}}$ are largely insignificant, with $\mathbf{B}_1{}^{(0)\mathrm{s}}$ the dominant mode of this degenerate pair for $R_\alpha > 2$.

Figures 11 and 12 show the poloidal and toroidal structures of the solution at $R_\alpha = R_{\alpha\,\mathrm{cr}}$.

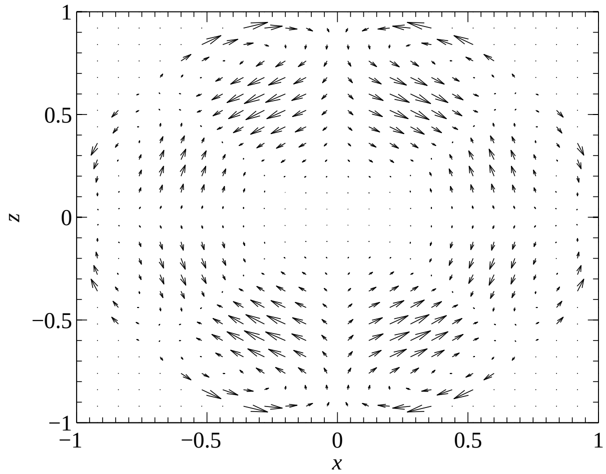

Figure 11: Magnetic field vectors in the (x, z)–plane of the quadrupolar poloidal field at $R_{\alpha\,\mathrm{cr}} \approx 0.14$ for the $\alpha^2\omega$ dynamo. As for Figure 8, vector length is proportional to $|\mathbf{B}|$.

The poloidal structure of the magnetic field at $R_\alpha = R_{\alpha\,\mathrm{cr}}$ is very similar to the mode $\mathbf{B}_3{}^{(0)\mathrm{s}}$ shown in Figure 5, the dominant poloidal mode at the growth threshold.

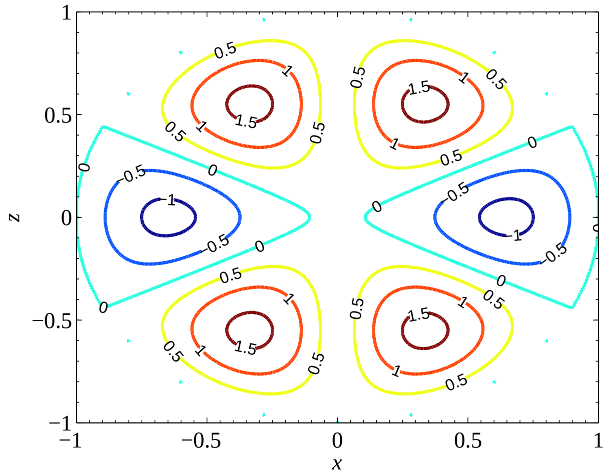

Figure 12: Contour representation in the (x, z)–plane of the strength of the quadrupolar toroidal field at $R_{\alpha\,\mathrm{cr}} \approx 0.14$ for the $\alpha^2\omega$ dynamo. The blue curves indicate the isolines for $B_\phi < 0$, the cyan curves indicate the isolines for $B_\phi = 0$ whilst the red and yellow curves indicate the isolines for $B_\phi > 0$. The isolines are drawn with increments of 0.5, for the values 0, ± 0.5, ± 1 and 1.5.

The toroidal structure is very similar to the dominant toroidal mode at the growth threshold, $\mathbf{B}_4{}^{(0)\mathrm{s}}$ shown in Figure 5, in a manner similar to that of the corresponding poloidal structure.

4.3 $\alpha\omega$ Dynamo

4.3.1 Antisymmetric Modes

We shall now consider the dipolar solution for the $\alpha\omega$ dynamo and compare this to the corresponding solution for the $\alpha^2\omega$ dynamo. The dependence of Re Γ and Im Γ on R_α is shown in Figure 13.

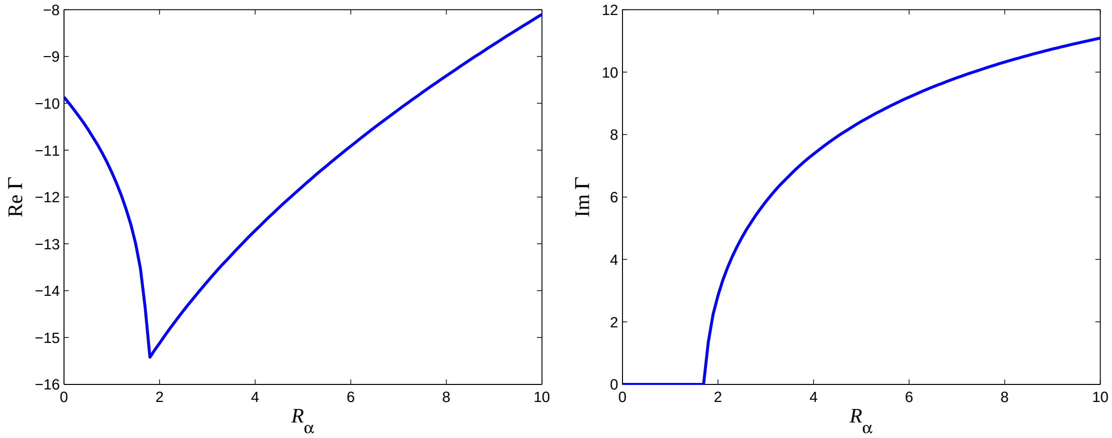

Figure 13: The dominant growth rate Re Γ and associated oscillation frequency Im Γ against R_α for the antisymmetric modes for the $\alpha\omega$ dynamo. Re $\Gamma < 0$ for the given range of R_α and so there is no realistic value for $R_{\alpha\,\mathrm{cr}}$.

Similar to Figure 6, the dominant growth rate initially decreases with R_α, with a turning point at $R_\alpha \approx 2$ at which Re Γ increases, but at a lower rate than for the $\alpha^2\omega$ dynamo solution. In contrast to Figure 6, Re $\Gamma < 0$ for the range of R_α considered. Hence, an $\alpha\omega$ dynamo will not produce a growing dipolar field for this model.

As for Figure 6, Im $\Gamma = 0$ for low values of R_α, with the modes becoming oscillatory as Re Γ increases. However, Im Γ increases continuously as Re Γ increases, in contrast to the $\alpha^2\omega$ dynamo solution.

The large differences between the dipolar solutions solutions for the $\alpha\omega$ and $\alpha^2\omega$ dynamos suggest that, for the antisymmetric modes, the $\nabla \times (\alpha \mathbf{B}_P)$ term is significant in (4.7). Hence the $\alpha\omega$ approximation in this case would be questionable.

4.3.2 Symmetric Modes

We shall now compare the quadrupolar solutions for the $\alpha^2\omega$ and $\alpha\omega$ dynamos. The dependence of Re Γ on R_α for the four symmetric modes is shown in Figure 14.

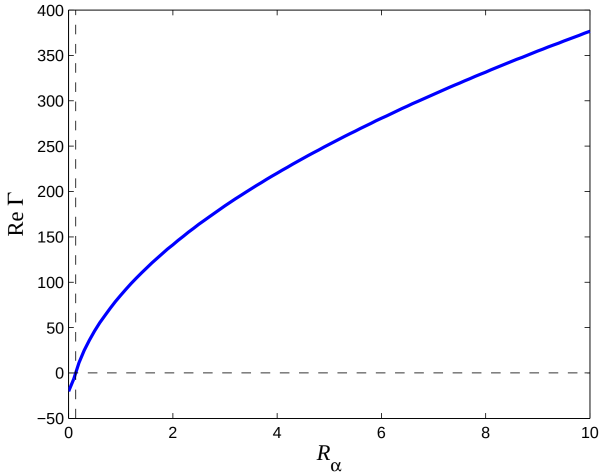

Figure 14: The dominant growth rate Re Γ against R_α for the symmetric modes for the $\alpha\omega$ dynamo. As for Figures 6 and 9, the vertical dashed line denotes $R_{\alpha\,\mathrm{cr}}$. As for the corresponding $\alpha^2\omega$ solution, Im $\Gamma = 0$ for all R_α.

This figure is remarkably similar to Figure 9. The growth rate increases rapidly with R_α, although at a lower rate than in Figure 9. Similar to the $\alpha^2\omega$ dynamo solution, the growth threshold for the symmetric modes i $R_{\alpha\,\mathrm{cr}} \approx 0.14$. From Figures 13 and 14, we conclude that $\alpha\omega$ dynamo action for this model results only in a growing quadrupolar field. As for the $\alpha^2\omega$ dynamo solution, the oscillation frequency is zero for all R_α and so the growing symmetric mode is stationary.

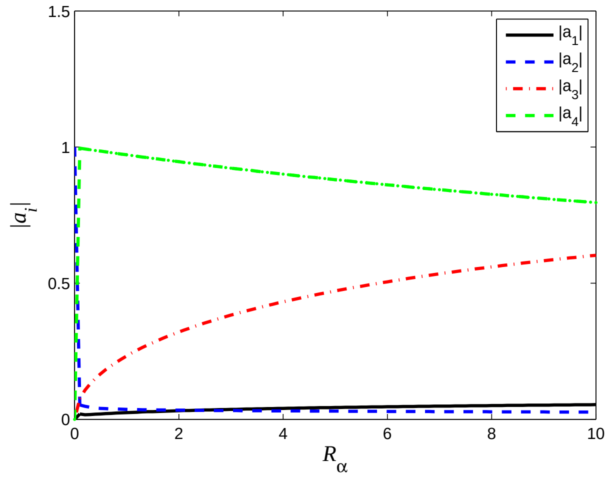

Figure 15: The normalised expansion coefficients $|a_i|$ against R_α for the symmetric modes. The lines denote the same coefficients as in Figure 10.

Figure 15 shows remarkable similarities between the dependence of the $|a_i|$ on R_α for the solutions for both dynamos. Again $\mathbf{B}_4{}^{(0)\mathrm{s}}$ is the dominant mode, except for very small R_α, with $\mathbf{B}_3{}^{(0)\mathrm{s}}$ increasing in significance with $R_{\alpha\,\mathrm{cr}}$. The other two modes are again largely insignificant.

We now examine the show the poloidal and toroidal structures of the solution at $R_\alpha = R_{\alpha\,\mathrm{cr}}$. From the earlier results of our analysis, the expectation is that the structures will be very similar to Figures 11 and 12.

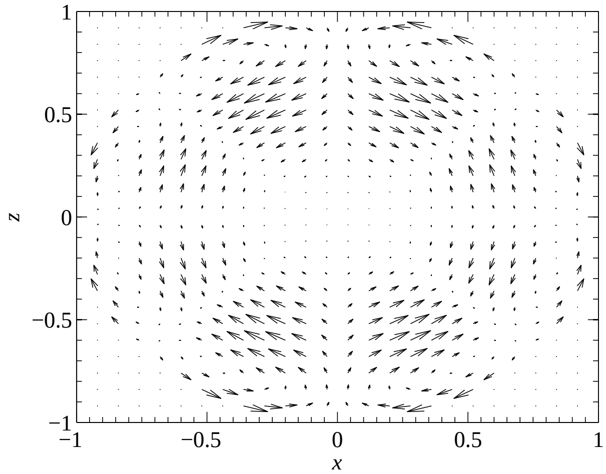

Figure 16: Magnetic field vectors in the (x, z)–plane of the quadrupolar poloidal field at $R_{\alpha\,\mathrm{cr}} \approx 0.14$ for the $\alpha\omega$ dynamo. As for Figures 8 and 11, the vector length is proportional to $|\mathbf{B}|$.

As shown in Figure 16, the poloidal magnetic field structure at $R_\alpha = R_{\alpha\,\mathrm{cr}}$ is very similar to $\mathbf{B}_3{}^{(0)\mathrm{s}}$, the same structure as in Figure 11.

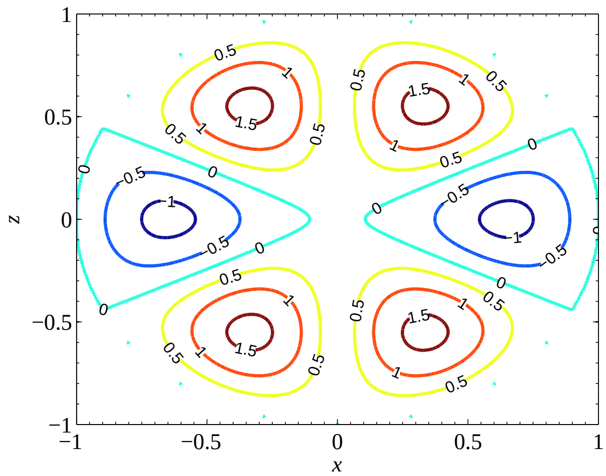

Figure 17: Contour representation in the (x, z)–plane of the strength of the quadrupolar toroidal field at $R_{\alpha\,\mathrm{cr}} \approx 0.14$ for the $\alpha\omega$ dynamo. The curves indicate the same isolines as in Figure 12.

Figure 17 shows that the toroidal magnetic field structure at $R_\alpha = R_{\alpha\,\mathrm{cr}}$ is very similar to $\mathbf{B}_4{}^{(0)\mathrm{s}}$. As for Figure 16, this is the same structure as shown in the corresponding figure in Section 4.2.2, Figure 12.

The similarities between the quadrupolar solutions for both dynamos suggest that, for the symmetric modes, the removal of the α effect as a possible source term for the toroidal field makes little difference. Hence, the $\nabla\times(\alpha\mathbf{B}_P)$ term can be ignored in (4.7) and so the $\alpha\omega$ approximation may be valid for this model.

5 Dynamo in an Embedded Disc

We shall now consider a more complicated model, where a flat disc is embedded into a spherical halo. For this purpose, we consider an α effect mostly confined to the disc of the form: $\alpha = \sin^2\theta\cos\theta$. A comparison of the two forms of α is shown in Figure 18.

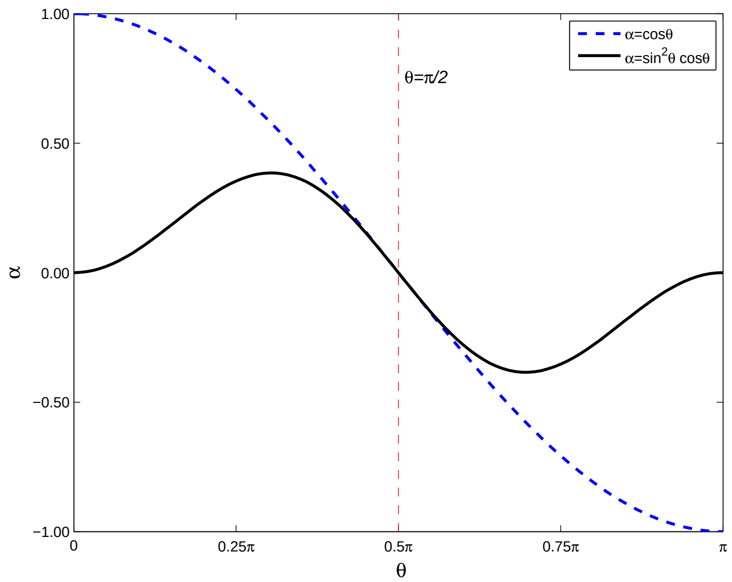

Figure 18: The two forms of α: $\cos\theta$ (blue, dashed) and $\sin^2\theta\cos\theta$ (black, solid). The dashed red line $\theta = \pi/2$ denotes the mid-plane.

For the quasi-homogeneous spherical dynamo model, α is concentrated near the poles and is close to zero near $\theta = \pi/2$. Whereas for the disc-halo model, α is maximum close to $\pi/2$ and is close to zero near the poles, which more closely resembles a disc.

For the disc-halo model, we shall perform the same analysis that was conducted in Section 4. We shall take the same parameters values $s_0 = 0.5$ and $R_\omega = 200$. The sole parameter will again be $0 \leq R_\alpha \leq 10$. We will use the same velocity field as before and consider the same sets of modes.

5.1 $\alpha^2\omega$ Dynamo

5.1.1 Antisymmetric Modes

Our analysis again focuses on the most rapidly growing field and we shall compare the following results to those in Section 4.2.1. The dependence of Re Γ and the associated oscillation frequency Im Γ on R_α for the four antisymmetric modes is shown in Figure 19.

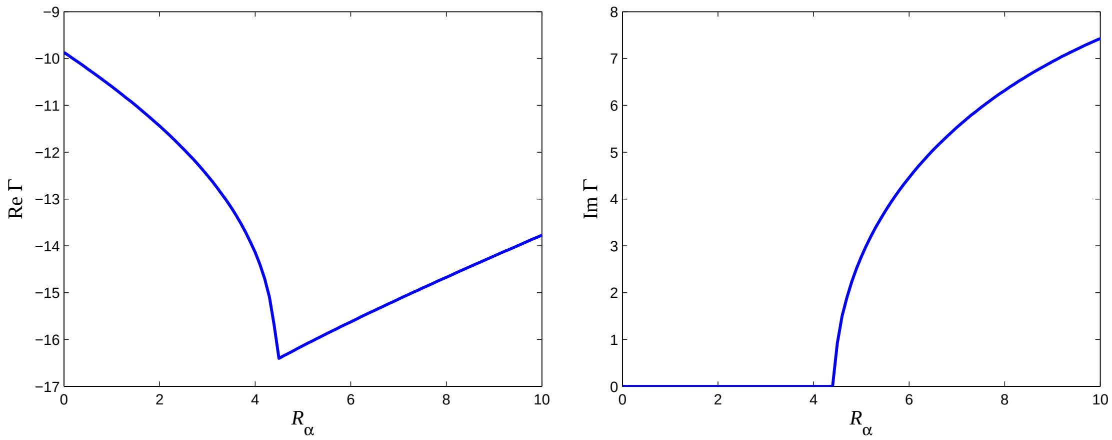

Figure 19: The dominant growth rate Re Γ and associated oscillation frequency Im Γ against R_α for the antisymmetric modes. As for Figure 13, the value of $R_{\alpha\,\mathrm{cr}}$ occurs outside the given range of R_α.

As for Figure 6, we see that whilst there is an initial decrease in the growth rate with R_α , but the turning point is at $R_\alpha \approx 4$. In addition, the rate of increase is much less than in Figure 6 and Re $\Gamma < 0$ for all R_α. Hence we conclude that for this model, $\alpha^2\omega$ dynamo action does not result in a growing dipolar field.

In the range of R_α for which the growth rate decreases, Im $\Gamma = 0$ and the magnetic field evolves. As Re Γ increases, the modes become oscillatory, and Im Γ increases with R_α. We are unable to fully compare the behaviour of Im Γ shown in this figure to Figure 6, since we have no data about the dependence of Im Γ on R_α for $R_{\alpha\,\mathrm{cr}}$.

This result is quite surprising considering that the corresponding case for the simple halo model did result in a growing magnetic field, albeit for large values of R_α. However, an possible explanation is that the form of α for this model is restricted, relative to $\alpha = \cos\theta$, since the maximum of $\sin^2\theta\cos\theta$ is approximately 0.4 compared to 1 for $\cos\theta$. Thus, we may expect that a larger value of R_α is required for a growing magnetic field.

5.1.2 Symmetric Modes

We now compare the quadrupolar solution for the $\alpha^2\omega$ dynamo in the disc-halo model with those in Section 4.2.2. The dependence of the dominant growth rate Re Γ on R_α for the symmetric modes is shown below.

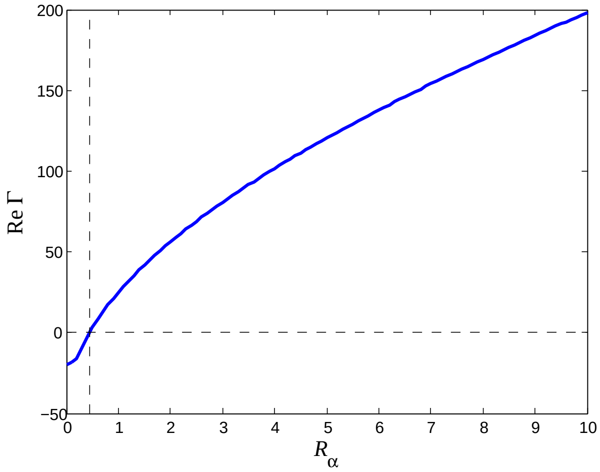

Figure 20: The dominant growth rate Re Γ against R_α for the symmetric modes. As in the previous section, the vertical dashed line denotes $R_{\alpha\,\mathrm{cr}}$. As in Section 4.2.1, Im $\Gamma = 0$ for all R_α.

As shown in Figure 20, the growth rate increases rapidly with R_α, similar to Figure 9. However, the rate of increase is lower, particularly for small R_α. The growth threshold for the symmetric modes is $R_{\alpha\,\mathrm{cr}} \approx 0.45$, significantly higher than for the $\alpha = \cos\theta$ model. Hence, we conclude that $\alpha^2\omega$ action does result in a growing quadrupolar field, albeit at larger values of R_α, and so the parity of the growing magnetic field is quadrupolar. As discussed in Section 5.1.1, the higher value of $R_{\alpha\,\mathrm{cr}}$ might be expected.

As for the quasi-homogeneous model, Im $\Gamma = 0$ for all R_α and so the growing quadrupolar mode is stationary.

To determine any differences between the quadrupolar $\alpha^2\omega$ dynamo solutions for both models, we examine the dependence of the moduli of the expansion coefficients $|a_i|$ on R_α, shown in Figure 21. This figure is very similar to Figure 10, except that $\mathbf{B}_2{}^{(0)\mathrm{s}}$ is the dominant mode of the largely insignificant pair. This is unlikely to affect the structure of the solution at at $R_{\alpha\,\mathrm{cr}}$, since $\mathbf{B}_4{}^{(0)\mathrm{s}}$ is much more prominent at the onset of magnetic field growth.

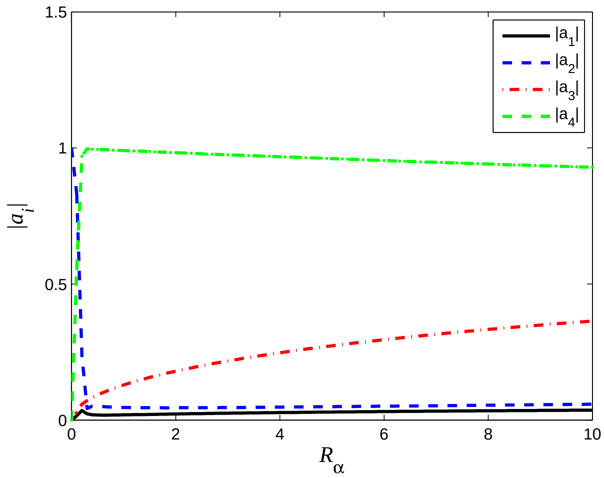

Figure 21: The normalised expansion coefficients $|a_i|$ against R_α for the symmetric modes. The lines denote the same coefficients as in Figures 10 and 15.

We now analyse the structure of the poloidal and toroidal fields at $R_\alpha = R_{\alpha\text{cr}}$, with the expectation that the results will be very similar to those in Figures 11 and 12.

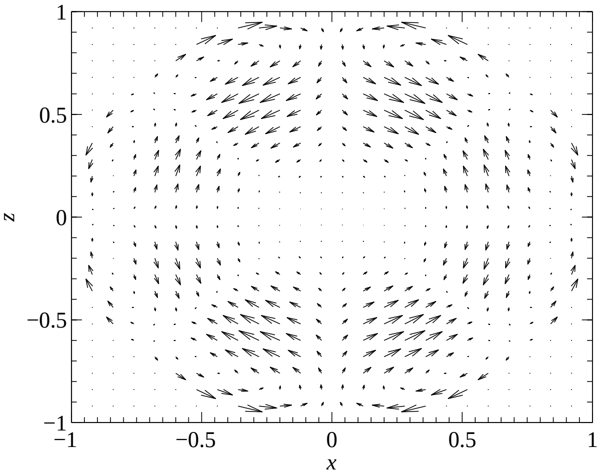

Figure 22: Vector representation in the (x, z)–plane of the quadrupolar poloidal field at $R_{\alpha\,\text{cr}} \approx 0.45$. As for the previous poloidal structure plots, the vector length is proportional to $|\mathbf{B}|$.

As shown in Figure 22, the poloidal magnetic field structure at $R_\alpha = R_{\alpha\,\text{cr}}$ is very similar to $\mathbf{B}_3{}^{(0)\text{s}}$, the dominant poloidal mode at the growth threshold. Likewise, Figure 23 shows that the structure of the toroidal magnetic field structure at $R_\alpha = R_{\alpha\,\text{cr}}$ is very similar to the dominant toroidal mode at the growth threshold, $\mathbf{B}_4{}^{(0)\text{s}}$. These structures are as expected from the results shown in Figure 21.

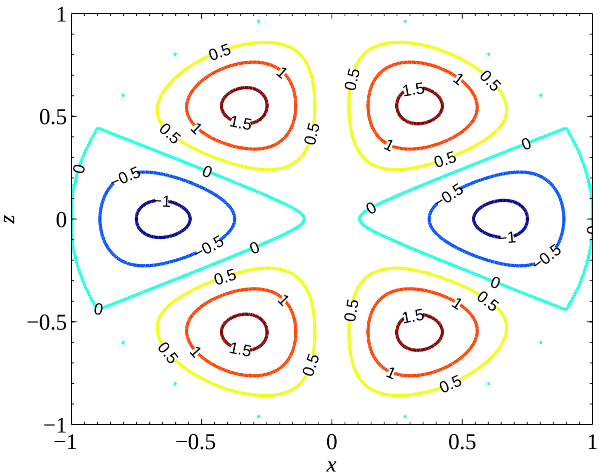

Figure 23: Contour representation in the (x, z)–plane of the strength of the quadrupolar toroidal field at $R_{\alpha\,\mathrm{cr}} = 0.45$ for the $\alpha^2\omega$ dynamo. The curves indicate the same isolines as in Figures 12 and 17.

Therefore, for the disc-halo model, we see that $\alpha^2\omega$ dynamo action results in only a growing quadrupolar field at a higher growth threshold. This field has the same structure as for the quasi-homogeneous model.

5.2 $\alpha\omega$ Dynamo

5.2.1 Antisymmetric Modes

We now consider the dipolar solution for the $\alpha\omega$ and compare the results to those in Section 4.3.1. The dependence of both the dominant growth rate Re Γ and associated oscillation frequency Im Γ are shown in Figure 24

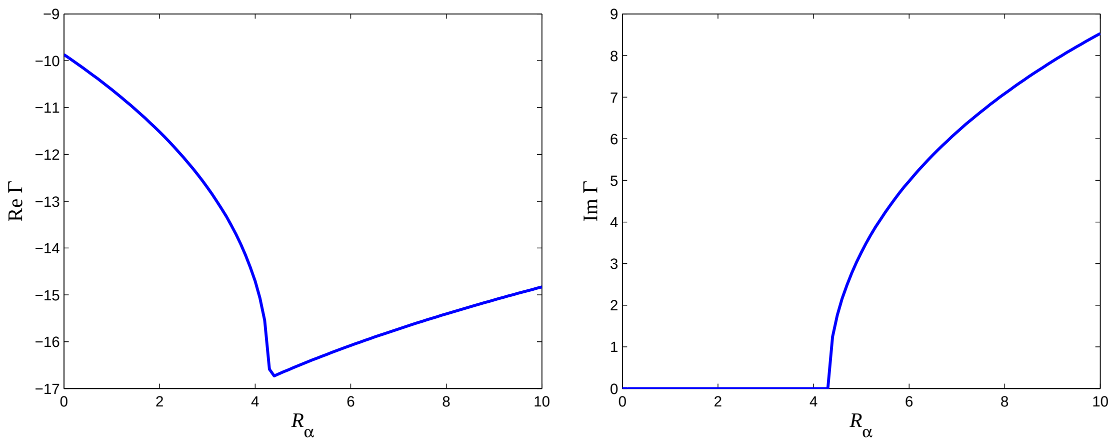

Figure 24: The dominant growth rate Re Γ and associated oscillation frequency Im Γ against R_α for the antisymmetric modes for the $\alpha\omega$ dynamo. As for Figures 13 and 19, the value of $R_{\alpha\,\mathrm{cr}}$ occurs outside the given range of R_α.

These graphs have similarities to those in Figure 13. The growth rate again initially decreases with R_α, but the turning point at $R_\alpha \approx 4$ at which Re Γ increases, which is close to the behaviour show in Figure 19. As for Figures 13 and 19, Re $\Gamma < 0$ in the considered range of R_α. Thus, for the disc-halo model, $\alpha\omega$ dynamo action does not result in a growing dipolar field, as for the $\alpha^2\omega$ dynamo. The modes become oscillatory as Re Γ increases, with the oscillation frequency increasing with R_α, similar to Figures 13 and 19.

The behaviour of both dipolar solutions is very similar for the disc-halo model. However commenting on the validity of the $\alpha\omega$ approximation may not be appropriate, as the region of R_α used does not correspond to any interesting behaviour, such as magnetic field growth, for either dynamo.

5.2.2 Symmetric Modes

Finally, we consider the quadrupolar $\alpha\omega$ dynamo solution, with a view to comparing the results to those in Section 4.3.2. In addition, we shall examine if the disc-halo model produces any appreciable differences between the two dynamo solutions. We examine the dependence of the dominant growth rate Re Γ for the four symmetric modes on R_α, shown below.

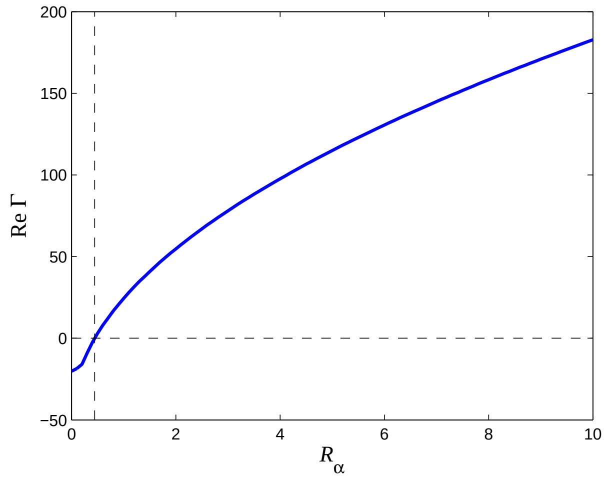

Figure 25: The dominant growth rate Re Γ against R_α for the symmetric modes. As for the previous figures, the vertical dashed line denotes $R_{\alpha\,\mathrm{cr}}$. Im $\Gamma = 0$ for all R_α.

As for Figure 14 in comparison to Figure 9, the similarities between Figures 25 and 20 are significant. Re Γ increases rapidly with R_α, although at a lower rate than for the previous figures. As for Figure 20, the growth threshold is $R_\alpha \approx 0.45$. The growing mode is again stationary, as Im $\Gamma = 0$ throughout the range considered for R_α.

To determine any discrepancies between the two dynamo solutions, we examine the dependence of the moduli of the expansion coefficients $|a_i|$ on R_α, shown in Figure 26. The results for the coefficients for the two dynamo solutions are almost identical, with a small exception in that the significance of the the modes $\mathbf{B}_1{}^{(0)\mathrm{s}}$ and $\mathbf{B}_2{}^{(0)\mathrm{s}}$ in this figure is closer to those shown in the corresponding figures in Section 4.

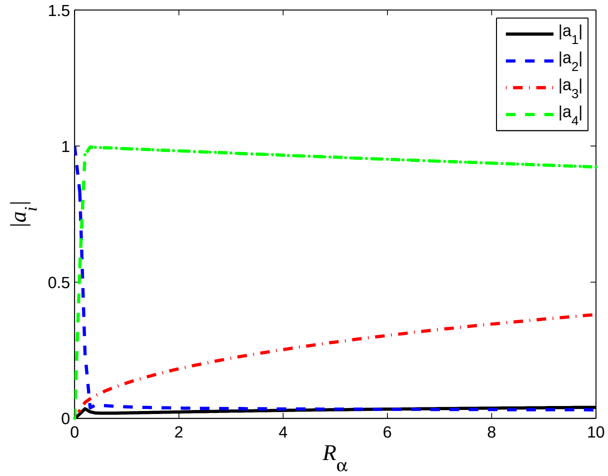

Figure 26: The normalised expansion coefficients $|a_i|$ against R_α for the symmetric modes. The lines denote the same coefficients as previously discussed.

We finish our analysis by examining the structures of the poloidal and toroidal fields at $R_\alpha = R_{\alpha\mathrm{cr}}$, shown below. From Figure 26, we except the structures to be similar to those shown in Figures 22 and 23.

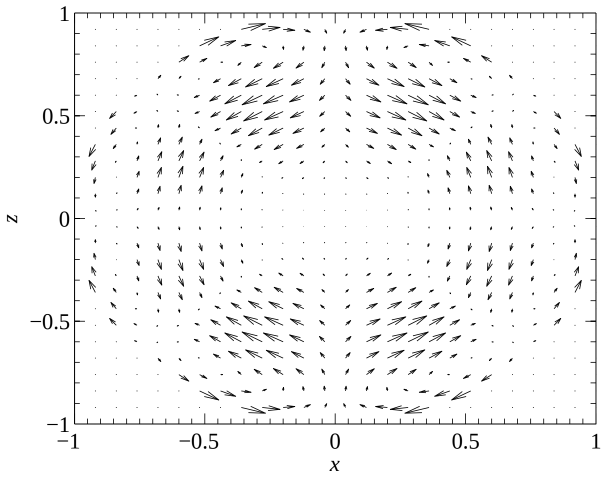

Figure 27: Vector representation in the (x, z)–plane of the quadrupolar poloidal field at $R_{\alpha\,\mathrm{cr}} \approx 0.45$. As for the previous quiver plots, the vector length is proportional to $|\mathbf{B}|$.

As shown in Figures 27 and 28, we see the same structures for the poloidal and toroidal fields as in Figures 22 and 23, with the poloidal and toroidal fields very similar to $\mathbf{B}_3{}^{(0)\mathrm{s}}$ and $\mathbf{B}_4{}^{(0)\mathrm{s}}$ respectively. This is also the same structure as shown in the corresponding figures for the quasi-homogeneous model.

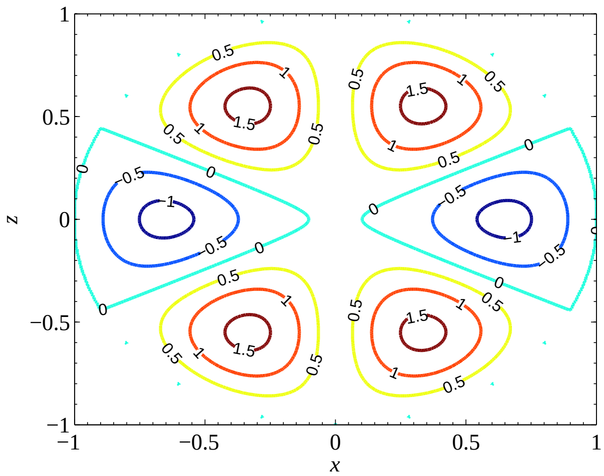

Figure 28: Contour representation in the (x, z)–plane of the quadrupolar toroidal field at $R_{\alpha\,\mathrm{cr}} \approx 0.45$ for the $\alpha^2\omega$ dynamo. The curves indicate the same isolines as in Figures 12, 17 and 23.

Thus, because of the similarities between the two dynamo solutions for the symmetric modes, the consequences of removing the α effect as a source term for the toroidal field appears to be small. Hence, as for the quasi-homogeneous model, we may ignore the $\nabla \times (\alpha \mathbf{B}_P)$ term in (4.7), and so the $\alpha\omega$ approximation appears to be valid.

Therefore, we can conclude that $\alpha^2\omega$ and $\alpha\omega$ dynamos in the disc-halo model results only in a growing quadrupolar field, with a higher growth threshold than for the quasi-homogeneous model. The structure of the growing field is similar to that for the quasi-homogeneous model.

6 Conclusion

We have discussed dynamo action for two models; a galactic halo and a more complicated disc-halo system. For each model, we have discussed both the $\alpha\omega$ and $\alpha^2\omega$ dynamos for modes of both dipolar and quadrupolar parity.

In both models, we have found that the preferred symmetry of the magnetic field in the halo is quadrupolar, the same as for galactic discs [11]. With the exception of the $\alpha^2\omega$ dynamo solutions for the simple halo model, self-excitation occurs only for the quadrupolar field. For this case, a comparison

$R_{\alpha\mathrm{cr}}$ shows that for the symmetric modes, $R_{\alpha\mathrm{cr}}$ is approximately a factor of 50 smaller than the corresponding value for the antisymmetric modes. Since a lower value of $R_{\alpha\mathrm{cr}}$ indicates the preferred symmetry, this again confirms that quadrupolar fields dominate. The apparent cause for this preference is the cylindrical geometry of the rotational velocity, akin to the rotation of galaxies.

The embedding of a disc into the halo results in a greater dominance for the quadrupolar mode, although the structures of such fields are largely unaffected. This feature of the solution, which needs additional confirmation with further study, will have significant implications for the symmetries of magnetic fields in the disc-halo systems of spiral galaxies.

In the cases where we found magnetic field growth, the growing modes are steady, whilst decaying antisymmetric modes, for the most part, are oscillatory. For the symmetric modes, the similarity of the two dynamo solutions for both models indicate that for the symmetric modes, the ω effect is dominant. By contrast, we can infer from the results in Sections 4.2.1 and 4.3.1 that the α effect is more prominent for the antisymmetric modes.

Extending the range of R_α beyond that considered in the report for the antisymmetric $\alpha\omega$ dynamo solution for the simple halo model, yielded a critical dynamo number of $D_{cr} \sim 5.5 \times 10^3$, where $D = R_\alpha R_\omega$ for the $\alpha\omega$ dynamo. A dynamo model for T Tauri stars using similar forms of α and $\mathbf{V}$ yields a critical dynamo number $D_{cr} \sim 5 \times 10^3$ [12], in some with agreement our result.

6.1 Further Study

The model with an embedded disc is a step towards modeling a disc-halo system. However, it is still rather idealised and much more work is required to obtain a realistic model for the disc-halo system of a spiral galaxy. An important step is to introduce variable diffusivity $\eta(r, \theta)$, to account for different values of η in the disc and halo. This would require a modification to the given system of equations to allow for turbulent dimagnetism. In addition, the equations would have to account for integrals involving $\nabla\eta$ and those integrals that will no longer vanish as a result of a non-constant η. Another important modification will be to include a more complicated form for α, including a thinner disc and dependence on the cylindrical radius. These changes will require an increase in the number of free decay modes used in the expansion.

It may also be possible to apply the method discussed to a weakly non-linear system which incorporates quenching of both α and η, however this is likely to require changes to deeper aspects of the approach.

References

[1] R. Beck, Magnetic Fields in Galaxies, *Proceedings of the XXV Canary Islands Winter School of Astrophysics*, Edited by J. Sánchez Almeida and M. J. Martínez González, Cambridge University Press, Cambridge, 2013. Pages 3, 15, 21, 25-28 and 32-33.

[2] R. Beck, A. Brandenburg, D. Moss, A. Shukurov and D. Sokoloff, Galactic magnetism: recent developments and perspectives, *Annual Review, Astronomy and Astrophysics 34*, 1996.

[3] J. Binney and M. Merrifield, *Galactic Astronomy*, Edited by J. P. Ostriker and D. N. Spergel, Princeton University Press, Princeton, 1998. Pages 1, 210, 224-228, 451-459, 506 and 668.

[4] A. R. Choudhuri, *The Physics of Fluids and Plasmas*, Cambridge University Press, Cambridge, 1998. Pages 197-198 and 236.

[5] C. Jones, Dynamo Theory, *Dynamos, Volume LXXXVIII: Lecture Notes of the Les Houches Summer School 2007*, Edited by P. Cardin and L. G. Cugliandolo, Elsevier Science, 2007. Pages 7-8, 23, 38-39 and 44-46.

[6] F. Krause and K. H. Rädler, *Mean Field Magnetohydrodynamics and Dynamo Theory*, Pergamon Press, Oxford, 1980. Pages 172-175 and 178-180.

[7] M. Longair, *Galaxy Formation*, Springer, 2007. Pages 51 and 66-67.

[8] H. K. Moffat, *Magnetic Field Generation in Electrically Conducting Fluids*, Edited by G. K. Batchelor and J. W. Miles, Cambridge University Press, Cambridge, 1978. Pages 13, 20-21, 37-39, 109, 152 and 198-199.

[9] E. N. Parker, Magnetic fields in the cosmos, *Scientific American Volume 249*, Issue 2, 1983.

[10] K. H. Rädler, Mean-Field dynamo Theory: Early Ideas and Today's Problems, *Magnetohydrodynamics: Historical Evolution and Trends Part I*, Edited by S. Mokolov, R. Moreau, H. K. Moffat, Springer, 2007. Pages 59, 62-64.

[11] A. Shukurov, Mathematical Aspects of Natural Dynamos, *The Fluid Mechanics of Astrophysics and Geophysics*, Edited by E. Dormy and A. M. Soward, CRC Press, 2007. Pages 319-322, 325-326, 331-332, 335.

[12] D. D. Sokoloff, S. N. Nefedov, A .A. Ermash and S. A. Lamzin, Dynamo model with a small number of modes and magnetic activity of T Tauri stars, *Astronomy Letters*, Volume 34, 2008.

[13] R. J. Tayler, *Galaxies: Structure and Evolution*, Cambridge University Press, Cambridge, 1978. Pages 28-29.